**Polyamines buffer labile iron to suppress ferroptosis**

Pushkal Sharma[1,2], Maria-Eirini Pandelia[3], Heather R. Keys[1], Christalyn Ausler[1], Ryan P. Mansell[4,5], Jillian Stark[4,5], Sebastian Müller[6], Shinya Imada[4], Ivan S. Pires[2,4], Tenzin Kunchok[1], Millenia Waite[1], Bingbing Yuan[1], Amy Deik[7], Luke Ferro[1], Paula T. Hammond[2,4], Raphaël Rodriguez[6], Whitney S. Henry[4,5,8,*], Ankur Jain[1,5,9,*]

[1] Whitehead Institute for Biomedical Research, Cambridge, MA, USA

[2] Department of Chemical Engineering, Massachusetts Institute of Technology, Cambridge, MA, USA

[3] Department of Biochemistry, Brandeis University; Waltham, MA, USA

[4] Koch Institute for Integrative Cancer Research at MIT, Cambridge, MA, USA

[5] Department of Biology, Massachusetts Institute of Technology, Cambridge, MA, USA

[6] Institut Curie, CNRS, INSERM, PSL Research University, Paris, France

[7] Broad Institute of MIT and Harvard, Cambridge, MA, USA

[8] Howard Hughes Medical Institute, Cambridge, MA, 02139, USA

[9] Lead contact

[*] Correspondence: ajain@wi.mit.edu (A.J.), wshenry@mit.edu (W.S.H.)

**Summary**

Polyamines are essential and evolutionarily conserved metabolites present at millimolar concentrations in mammalian cells. Cells tightly regulate polyamine homeostasis through complex feedback mechanisms, yet the precise role necessitating this regulation remains unclear. Here, we show that polyamines function as endogenous buffers of redox-active iron, providing a molecular link between polyamine metabolism and ferroptosis. Using genome-wide CRISPR screens, we identified a synthetic lethal dependency between polyamine depletion and the key ferroptosis suppressor, GPX4. Mechanistically, we show that polyamine deficiency triggers a redistribution of cellular iron, increasing the labile iron pool and upregulating ferritin. To directly visualize this iron buffering in living cells, we developed a genetically encoded fluorescent reporter for redox-active iron. Live-cell analysis revealed a striking inverse correlation between intracellular polyamine levels and redox-active iron at single-cell resolution. These findings reposition polyamines as key regulators of iron homeostasis, with implications for ferroptosis-linked disease states and cellular redox balance.

## Introduction

Polyamines are essential, evolutionarily conserved metabolites found in nearly all living organisms[1]. In mammalian cells, the major polyamines are putrescine, spermidine, and spermine (Figure 1A). These metabolites are present at millimolar concentrations and exist predominantly in protonated forms, enabling extensive interactions with negatively charged biomolecules, particularly RNA[2]. Despite their abundance, the molecular functions of polyamines remain incompletely understood.

Cells invest heavily in regulating polyamine homeostasis through an elaborate feedback network involving biosynthesis, catabolism, and transport (Figure 1B). Ornithine decarboxylase (ODC1), the rate-limiting biosynthetic enzyme, has one of the shortest half-lives of any mammalian protein and is uniquely regulated by polyamine-induced expression of antizyme (OAZ1) via programmed +1 ribosomal frameshifting[3,4]. Polyamine catabolism and transport are similarly under intricate feedback control, enabling cells to rapidly adjust intracellular concentrations in response to perturbations[5,6]. This sophisticated regulatory architecture raises a central question: why do cells maintain polyamines at millimolar concentrations and encode such extensive regulatory machinery? The best-defined role of polyamines is the hypusination of eIF5A, a spermidine-dependent modification which is essential for translation[7]. However, hypusination requires sub-micromolar substrate concentrations[8,9] and does not explain the enormous metabolic investment in tightly regulating polyamine concentrations at millimolar levels. Polyamine dysregulation also affects diverse cellular processes including chromatin compaction[10], cell differentiation[11], tissue regeneration[12], autophagy[13], and immune function[14]. Polyamine levels decline with age, and dietary supplementation in model organisms improves memory[15], cardiac function[16], and lifespan[17]. Mutations in polyamine pathway genes cause disorders such as Parkinsonian syndromes[18], Snyder-Robinson syndrome[19] and Bachmann-Bupp syndrome[20], and elevated levels of polyamines are observed across many cancers[21]. These pleiotropic effects suggest additional molecular functions that remain largely undefined.

To identify cellular dependencies that emerge during polyamine stress, we performed a genome-wide CRISPR-Cas9 screen[22,23] in human cells under polyamine-depleted conditions. We reasoned that this approach would reveal synthetic lethal interactions, i.e., genes and pathways that become essential only when polyamine homeostasis is disrupted. Our screen revealed a surprising link between polyamines and iron homeostasis: polyamine depletion rendered cells highly dependent on GPX4 (glutathione

peroxidase 4), an antioxidant enzyme that protects membranes from lethal lipid peroxidation and ferroptotic cell death[24,25]. We found that this dependency stems from an increase in labile iron pools upon polyamine depletion. Using a combination of Mössbauer spectroscopy and $Fe^{2+}$-binding and competition assays, we show that polyamines chelate $Fe^{2+}$. To directly visualize this relationship, we developed a genetically encoded fluorescent reporter for redox-active iron. Single-cell analysis revealed that labile iron levels increase as polyamines decline, supporting a direct iron-buffering role. Our findings establish polyamines as endogenous iron buffers, a previously unrecognized function in redox homeostasis. This metabolic dependency creates a targetable vulnerability, opening new therapeutic avenues for inducing synthetic lethality through combined targeting of polyamine metabolism and ferroptotic pathways.

**CRISPR screen identifies genetic dependencies under polyamine depletion**

The polyamine biosynthetic pathway involves two rate-limiting steps: the formation of putrescine by ODC1, and the generation of aminopropyl donors by AMD1, which are then incorporated into spermidine and spermine[1]. Polyamine depletion using the ODC1 inhibitor DFMO or the AMD1 inhibitor sardomozide, induces cytostasis without causing substantial cell death (Figure 1C). To identify genetic dependencies under varying polyamine levels, we conducted a genome-wide CRISPR-Cas9 knockout screen in K562 cells (Figure 1D). Cells transduced with a CRISPR sgRNA library[26] targeting ~20,000 protein-coding genes (5 sgRNAs per gene) were cultured with or without DFMO for 14 days. Polyamine depletion following DFMO treatment was confirmed via enzymatic assay (Figure S1A), and sgRNA abundance was compared between treated and untreated conditions using the Robust Rank Aggregation (RRA) algorithm[27] (Table S1).

Most genes scored similarly across both conditions, but several displayed selective depletion or enrichment in DFMO-treated cells. Notably, loss of genes related to polyamine biosynthesis, including ODC1 and SMS (spermine synthase), sensitized cells to DFMO treatment, validating our screening approach (Figure 1E-F). This analysis identified ATP13A3, BCL2L1, and GPX4 as the top synthetic lethal hits, showing the strongest fitness defects (by p-value) upon polyamine depletion (Figure 1E-F). In contrast, knockout of the membrane proteins SLC3A2 and SLC7A6 enhanced survival under DFMO treatment (Figure 1F), likely reflecting their roles in polyamine export. SLC3A2 is an adapter protein

that regulates several amino acid transporters and promotes polyamine excretion[28]. SLC7A6 forms a complex with SLC3A2[29] and may similarly contribute to polyamine export.

The synthetic lethality of ATP13A3, a known polyamine transporter[30], likely reflects its role in the uptake of residual polyamines from the cell culture medium. Combined inhibition of polyamine synthesis (via DFMO) and transport (via ATP13A3 knockout) could fully deplete intracellular polyamines, inducing cell death. BCL2L1 and GPX4, two additional top hits, are key survival factors in distinct cell death pathways. BCL2L1 encodes an anti-apoptotic protein that has been shown to bind and regulate voltage-dependent anion channel (VDAC) and mitochondrial membrane potential[31]. GPX4 is a lipid quality control factor that inhibits phospholipid peroxidation, and is a central regulator of ferroptosis: an iron-dependent cell death pathway characterized by lipid peroxidation[24,25].

We validated these findings using sardomozide, another polyamine biosynthesis inhibitor which targets AMD1 and blocks spermidine and spermine synthesis (Figure 1B). Notably, this mechanism is distinct from that of DFMO, which targets ODC1 and inhibits putrescine production. Sardomozide induced substantial cytotoxicity in GPX4 knockout cells but not in control cells targeted at the AAVS1 safe-harbor locus (Figure 1G). GPX4 knockout cells proliferated slower than AAVS1 targeting cells (data not shown). Similarly, pharmacological inhibition of BCL2L1 with A-1331852 sensitized cells to polyamine depletion (Figure 1H). Notably, inhibition of GPX4 or BCL2L1 alone did not cause cell death, confirming synthetic lethality. Given the central role of GPX4 in preventing ferroptosis, we focused on understanding how polyamine depletion primes cells for this iron-dependent form of cell death.

**Polyamine depletion sensitizes cells to ferroptosis**

We next investigated the mechanism underlying synthetic lethality between polyamine depletion and GPX4 loss. Co-treatment with AMD1 inhibitor sardomozide and GPX4 inhibitors (ML162 or RSL3), led to substantial cell death whereas individual treatments did not (Figure 2A). Importantly, spermidine supplementation largely rescued sardomozide-induced cell death (Figure 2B), validating that the synthetic lethality results from on-target inhibition of polyamine biosynthesis. Because sardomozide is a polyamine analog (Figure S1B) and competes with spermidine for uptake (Figure S1C, see “Polyamine import measurements” in Methods), exogenous spermidine may not fully restore intracellular polyamine levels, potentially explaining the incomplete rescue. Interestingly, high concentrations of polyamines in

the medium re-sensitized cells to ferroptosis (Figure 2B), consistent with previous reports[32,33] (see below).

Building on our pharmacological data, we used genetic perturbations to dissect the contribution of individual polyamines to ferroptosis sensitivity. GPX4 inhibition induced substantial cell death in spermidine synthase (SRM) knock-out cells (Figure 2C) but not in control AAVS1-targeted cells. SRM knockout depletes both spermidine and spermine, resulting in the accumulation of the diamine putrescine. This vulnerability was rescued by spermidine supplementation, confirming the on-target activity of Cas9 (Figure 2D). In contrast, SMS (spermine synthase) knockout cells, which lack spermine but accumulate spermidine due to blocked conversion, were resistant to GPX4 inhibition (Figure 2C). SRM and SMS knockouts were confirmed by immunoblotting (Figure 2D). These results suggest that spermidine is sufficient to protect against ferroptosis, while putrescine alone cannot maintain viability under GPX4 inhibition. While spermine depletion alone does not sensitize cells to ferroptosis, its role under physiological conditions cannot be excluded.

We tested whether ferroptosis inhibitors could rescue cell death in polyamine-depleted cells. Treatment with known ferroptosis inhibitors, including lipophilic antioxidants[34] ferrostatin-1 and liproxstatin-1 (recently also shown to act as an iron chelator[35]), fully rescued GPX4 knockout cells from polyamine deprivation-induced death (Figure 2E). In contrast, inhibitors targeting other cell death pathways – such as apoptosis (z-VAD-FMK[36]), cuproptosis (tetrathiomolybdate[37]), and general oxidative stress (cell-permeable glutathione) – were ineffective (Figure 2E). Peroxidized lipid levels, assessed using BODIPY-C11 probe[38], were comparable across untreated controls, polyamine-deficient cells (sardomozide-treated), and GPX4 knockout cells (Figure 2F). However, brief GPX4 inhibition (~3 h, ML162) in polyamine-deficient cells markedly increased lipid peroxidation, consistent with ferroptotic lipid damage (Figure 2F). This synthetic lethal relationship was observed across multiple cell types: polyamine depletion enhanced ferroptosis sensitivity in NOMO (human monocytic leukemia) and HEL (human erythroleukemia) and MEL (mouse erythroleukemia) cells (Figure 2G-H, Figure S1D). Collectively, these results establish that polyamine depletion, specifically the loss of spermidine and spermine, creates a metabolic state selectively vulnerable to ferroptosis.

**Effects of polyamines are independent of major ferroptosis regulators**

Having established that polyamine depletion sensitizes cells to ferroptosis, we next sought to understand the underlying mechanism. Notably, while our data demonstrate that polyamine depletion sensitizes cells to ferroptosis, recent studies report that excess intracellular polyamines can also promote ferroptosis, likely through a different route. Excess spermidine and spermine are catabolized by the enzymes spermine oxidase (SMOX) and polyamine oxidase (PAOX), which convert them into lower-order polyamines such as putrescine while generating hydrogen peroxide and reactive aldehydes as byproducts[33]. These reactive intermediates can propagate lipid peroxidation, thereby sensitizing cells to ferroptotic cell death[32,39]. We therefore examined whether polyamine levels exhibit a biphasic relationship with ferroptosis sensitivity. Consistent with previous reports, we found that high-dose spermidine supplementation (100 μM) increased susceptibility of GPX4 inhibition. In sharp contrast, lower concentrations used in our rescue experiments (10 μM), which are closer to the physiological extracellular levels[40], were protective (Figure 3A). These findings indicate that both polyamine excess and deficiency can sensitize cells to ferroptosis, but likely through distinct biochemical routes, emphasizing that tight regulation of polyamine homeostasis is critical for redox balance.

We next asked whether polyamine depletion sensitizes cells to ferroptosis through disruption of polyamine-dependent cellular processes. Spermidine is required for an essential post-translational modification, hypusination, of eIF5A. Hypusinated eIF5A plays multiple roles in mRNA translation including elongation, termination, and start codon selection[41,42]. If reduced hypusination was responsible for ferroptosis sensitivity, then polyamine depletion would be expected to decrease hypusinated eIF5A levels. However, immunoblot analysis revealed that acute sardomozide treatment under our assay conditions maintained normal levels of hypusinated eIF5A (Figure 3B), likely because the existing hypusinated pool is stable and cellular spermidine was incompletely depleted. Notably, direct hypusination blockade with GC7 did sensitize cells to ML162-induced ferroptosis, an effect rescued by liproxstatin-1 (Figure S1E). This suggests that while chronic hypusination loss can promote ferroptosis, it does not explain the acute effects of polyamine depletion in our system. Polyamine depletion has also been reported to induce cell-cycle arrest[43]. Because G1/S arrest can sensitize cells to ferroptosis in specific contexts via downregulation of phospholipid remodeling enzymes[44], we tested whether cell-cycle arrest alone could account for the ferroptosis phenotype. Pharmacologic G1 arrest with palbociclib effectively blocked cell-cycle progression (Figure S1F) but did not sensitize cells to ML162-induced

ferroptosis (Figure S1G), indicating that cell-cycle inhibition per se is not sufficient to explain the increased ferroptosis sensitivity in this system.

We then asked whether polyamine depletion sensitizes cells to ferroptosis by altering the expression or activity of known ferroptosis regulators. Besides GPX4, two key regulators of the ferroptosis pathway are: ACSL4 (acyl-CoA synthetase long-chain family member 4) which enriches membranes with polyunsaturated fatty acids that serve as peroxidation substrates[45], and FSP1 (ferroptosis suppressor protein 1) which suppresses ferroptosis by regenerating ubiquinol, a lipid-soluble antioxidant that scavenges lipid peroxyl radical[46,47]. Western blot analysis revealed that the levels of ACSL4 and FSP1 were largely unchanged by polyamine depletion (Figure 3C-D). To test whether polyamines might nevertheless modulate FSP1 activity independently of its abundance, we treated GPX4 knockout cells with the FSP1 inhibitor iFSP1. This had no effect on cell viability (Figure 3E), indicating that impaired FSP1 function does not explain the ferroptosis sensitivity induced by polyamine depletion. Interestingly, GPX4 expression increased upon polyamine depletion (Figure 3C, bottom), likely reflecting a compensatory response to heightened ferroptosis vulnerability.

Previous studies have suggested that polyamines may function as antioxidants[48], raising the possibility that their depletion sensitizes cells to ferroptosis by removing a radical-scavenging species. To test this possibility, we used the fluorescence-enabled inhibited autoxidation (FENIX) assay[49], which monitors lipid peroxidation in native liposomes by tracking the oxidation of STY-BODIPY, a lipophilic fluorophore that is quenched upon reaction with lipid peroxyl radicals. Radical-trapping antioxidants (RTAs) compete with STY-BODIPY, thereby preserving fluorescence. Under our experimental conditions, polyamines did not exhibit any measurable lipid radical trapping activity (Figure 3F, Figure S1H). In contrast, PMC (2,2,5,7,8-pentamethyl-6-chromanol), a truncated vitamin E analog, robustly preserved fluorescence by intercepting lipid peroxyl radicals as expected (Figure 3F). These data indicate that direct radical scavenging by polyamines does not account for the ferroptosis sensitivity observed upon their depletion.

We then asked whether polyamine depletion compromises endogenous RTA pools. Untargeted metabolomics revealed that levels of NADPH, cysteine, and glutathione were largely unchanged upon polyamine depletion (Figure S1I), indicating that polyamine depletion does not measurably compromise these canonical antioxidant pools. Because hydrophobic RTAs such as vitamin K and cholesterol-

derived antioxidants are not reliably captured by standard metabolomics workflows, we instead examined these pathways at the transcriptional level. We observed no major changes in the biosynthetic or salvage pathways of vitamin K, 7-dehydrocholesterol, coenzyme Q10, or tocopherol (Figure S1J-M). Consistent with this, inhibition of vitamin K activation with warfarin[50] did not increase sensitivity to GPX4 inhibition (Figure 3G), indicating that vitamin K-dependent RTAs do not account for the ferroptosis sensitization observed upon polyamine depletion. Together, these results indicate that ferroptosis sensitization upon polyamine depletion is not mediated by compromised RTA pathways. Metabolomic profiling also revealed activation of the pentose phosphate pathway, reflected by increased levels of glucose-6-phosphate, 6-phosphogluconate, and downstream pentose intermediates, without a corresponding expansion of the NADPH pool (Figure S2A). This metabolic pattern, where NADPH consumption outpaces production, is a signature of elevated redox demand[51], suggesting that polyamine depletion increases oxidative burden through a mechanism other than RTA depletion.

Collectively, these experiments demonstrate that the ferroptosis-sensitizing effects of polyamine depletion are not mediated by canonical ferroptosis regulators (ACSL4 or FSP1), impaired hypusination of eIF5A, cell cycle arrest, or compromised RTA pathways. Polyamine depletion is associated with elevated redox demand, yet polyamines themselves lack radical-scavenging activity. While we cannot fully exclude contributions from these pathways, our findings strongly suggest that polyamine deficiency enhances ferroptosis susceptibility through a mechanism distinct from these established routes.

**Polyamine deficiency increases redox-active iron in cells**

Having established that polyamines protect against ferroptosis through a mechanism independent of known regulatory pathways, we next examined upstream processes that might explain this vulnerability. Given that ferroptosis is fundamentally driven by iron-catalyzed lipid peroxidation, we examined cellular iron homeostasis. Polyamine depletion using sardomozide resulted in a dramatic increase in levels of ferritin (FTH1), the principal iron storage protein[52,53] (Figure 4A). This induction mirrored the response to exogenous iron supplementation, such as with ferric ammonium citrate (FAC) or ferrous ammonium sulfate (FAS) (Figure S2B). Similar ferritin upregulation was observed upon SRM knock out and was reversed by exogenous spermidine supplementation (Figure 4B), supporting that the ferritin response results from polyamine loss. Likewise, quantitative proteomics showed a modest but coherent

induction of numerous proteins involved in maintaining iron homeostasis (e.g., FTL, CISD1, BOLA2, Figure S2C-D), consistent with increased iron stress in polyamine depletion condition.

Ferritin sequesters iron in an insoluble, non-reactive form, mitigating the risk of excessive redox-active iron accumulation[54]. We hypothesized that ferritin upregulation in polyamine-deficient cells represents an adaptive response to increased redox-active iron. Supporting this hypothesis, treatment with deferoxamine (DFO), an iron chelator, blunted the increase in ferritin levels from polyamine depletion (Figure 4C). We next tested whether elevated redox-active iron is functionally responsible for GPX4 dependence. DFO treatment restored viability in polyamine-deficient cells (either treated with sardomozide or lacking SRM) challenged with the GPX4 inhibitor ML162 (Figure 4D-E), supporting increased labile iron as a key driver of ferroptosis susceptibility. Conversely, increasing the redox-active iron pool using FAC supplementation induced cell death specifically in GPX4 knockout cells, and this effect was fully rescued by the ferroptosis inhibitor liproxstatin-1 (Figure 4F). Importantly, FAC had no impact on the viability of cells with functional GPX4 (Figure 4F), indicating that excess iron is not inherently toxic but becomes lethal when lipid peroxide repair is compromised. Collectively, these findings strongly implicate increased redox-active iron accumulation as a critical mediator of ferroptosis under polyamine-deficient conditions.

We then investigated the source of increased intracellular redox-active iron. We first examined if polyamine depletion results in increased iron uptake from the culture medium. Interestingly, total intracellular iron levels, as measured by inductively coupled plasma mass spectrometry (ICP-MS), showed negligible change upon polyamine depletion (Figure 4G). This observation indicates that the increase in the redox-active iron does not result from increased total iron but rather reflects a shift in the redox state or subcellular distribution of existing iron pools. Supporting this conclusion, ferritin levels were elevated even when polyamine-deficient cells were cultured in iron-free medium (IMDM) following extensive washing to remove extracellular iron (Figure 4H). Notably, this disruption of iron homeostasis was independent of changes in intracellular iron ligands, as polyamine depletion did not reduce the levels of established iron chelators[55], including glutathione, ATP, and citrate (Figure 4I).

Finally, we asked whether the disruption of iron homeostasis induced by polyamine depletion is conserved across cell types. Sardomozide treatment increased ferritin levels in U-2OS (osteosarcoma),

RPE-1 (retinal pigment epithelial) and MRC-5 (fetal lung fibroblast) cells (Figure 4J). Similarly, DFMO treatment elevated ferritin levels in mouse colon cancer organoids with *Apc* mutations (APC) alone or in combination with *Kras*$^{G12D}$, and *Trp53* mutations (AKP, a genotype observed in 40–45% of patients with colorectal cancers[56,57]) (Figure 4K). Consistent with a broader linkage between polyamine metabolism and iron programs, Cancer Dependency Map[58] showed a striking correlation between cellular dependencies on AMD1, a rate-limiting enzyme in polyamine biosynthesis, and TFRC (transferrin receptor), the major mediator of cellular iron import (Pearson's correlation coefficient, $r = 0.422$, across $n = 1149$ cell lines) (Figure 4M), with substantially stronger correlations in several lineages (e.g., prostate, $r=0.906$, $n=10$) (Figure S2E-I), indicating that cells with high iron demand (reflected by TFRC dependence) are especially reliance on robust polyamine synthesis.

**Genetically encoded iron sensor reveals polyamine-iron buffering in living cells**

Our biochemical and functional data support a model where polyamine depletion shifts intracellular iron toward a more redox-active state, potentially explaining the increased ferritin expression and ferroptosis sensitivity. To directly assess labile $Fe^{2+}$ levels in cells, we used the small-molecule ferrous iron probe RhoNox-1[59]. RhoNox-1 fluorescence increased upon polyamine depletion (Figure S3A-B), which was partially suppressed by the iron chelator DFO (Figure S3A-B), consistent with elevated labile $Fe^{2+}$ in polyamine-deficient cells. Likewise, RhoNox-M[60] confirmed elevated ferrous iron upon polyamine depletion (Figure S3C), similar to that observed upon ferrous ammonium sulfate (FAS) supplementation (Figure S3C). However, both probes exhibited substantial cell-to-cell variability, likely due to differences in probe uptake, leakage, and their preferential localization in acidic compartments[61]. More broadly, existing small-molecule iron probes often lack quantitative reliability, as their fluorescence signal is sensitive to local pH, ionic environment, and interference from other metals including zinc and copper. Furthermore, their limited cell permeability, poor photostability, and rapid clearance constrain their utility for quantitative single-cell analysis, long-term imaging, or use in complex tissues and organoids.

To overcome these limitations and directly test our hypothesis, we developed a genetically encoded reporter that quantifies redox-active iron in living cells with single-cell resolution. We harnessed the endogenous iron-responsive element (IRE)/iron regulatory protein (IRP) system: an evolutionarily conserved mechanism that exquisitely monitors and regulates the labile iron pool[62]. IRPs bind to IRE

hairpins in mRNAs encoding key iron regulatory proteins. When iron is low, IRP binding to 5′ UTR IREs (such as in ferritin and ferroportin mRNAs) blocks their translation, thus inhibiting iron sequestration and export[63]. Conversely, IRP binding to IREs in 3'UTRs (such as in transferrin receptor mRNA) enhance transcript stability and translation, thereby promoting iron uptake[64]. When labile iron concentrations rise, iron-sulfur clusters assemble on IRP1 while IRP2 undergoes degradation, releasing both proteins from their RNA targets and reversing this regulatory program.

We exploited this nature's own iron-sensing switch to engineer a genetically encoded fluorescent reporter (Figure 5A). We incorporated an optimized IRE configuration (Supplementary Note 1, Figure S3D–F) upstream of EBFP2 coding sequence. Translation initiation of EBFP2 depends directly on IRP release, providing a sensitive indicator of cellular redox-active iron. Additionally, we included an internal ribosome entry site (IRES)-mediated expression of EGFP downstream of EBFP2 as an internal normalization control, effectively accounting for cell-to-cell variability in mRNA abundance, transduction efficiency, and general translational status (Figure 5B). The fluorescence ratio of EBFP2 to EGFP provided a sensitive and quantitative measure of intracellular redox-active iron levels. Sensor expression was further refined by placement under a doxycycline-inducible promoter, enabling tight temporal control and preventing saturation of the sensor's dynamic range with prolonged expression. Importantly, reporter expression did not perturb endogenous iron metabolism, as evidenced by unchanged protein levels of iron metabolism enzymes, including FTH1, TFR1 and SLC40A1 (Figure S3G).

To validate the reporter, we measured changes in the fluorescence ratio (F = EBFP2/EGFP), normalized to untreated cells ($F_0$), to correct for imaging variations, as a function of redox-active iron. Treatment with the iron chelator DFO (100 μM, 48 h) markedly reduced this normalized fluorescence ratio in U-2OS cells by ~2.8 fold ($F/F_0 = 0.36 \pm 0.10$ compared to the baseline levels of $1.00 \pm 0.23$), consistent with reduced intracellular redox-active iron. Supplementation with ferric ammonium citrate (FAC, 10 mM, 18 h) partially restored the signal ($F/F_0 = 0.70 \pm 0.16$) (Figure 5C-D), confirming the sensor's responsiveness to iron availability. Similar trends were observed in K562 cells (Figure 5E), indicating the sensor functions across cell types.

We next leveraged our reporter to investigate the relationship between polyamine levels and redox-active iron. Treatment with sardomozide (5 μM for 48 h) or DFMO (0.5 mM for 48 h) led to a significant increase in $F/F_0$ (from 1.00 ± 0.23 to 2.22 ± 0.81 for sardomozide and 1.74 ± 0.45 for DFMO treatments respectively) (Figure 5F), indicating an increase in redox-active iron levels. Co-treatment with the iron chelator DFO (100 μM for 48h) reversed this elevation, confirming that the signal reflected iron-dependent changes (Figure 5F). Similar iron accumulation upon polyamine depletion was observed in K562 cells (Figure 5G), reinforcing the link between polyamine availability and the labile iron pools.

Furthermore, to definitively link these two metabolic pools at a single-cell level, we implemented a dual-reporter strategy. We co-expressed our iron sensor alongside a genetically encoded polyamine reporter we recently developed[65]. This sensor employs a polyamine-responsive ribosomal frameshifting region derived from OAZ1 gene cloned between two fluorescent proteins, mCherry and miRFP670-2 (Figure 5H). In this design, miRFP670-2 is produced only upon polyamine-stimulated frameshifting, providing a direct readout of intracellular polyamine concentrations, while mCherry serves as an internal normalization control. This dual-reporter approach enabled the simultaneous and quantitative measurement of both pathways within individual cells. We treated cells with a titration of sardomozide to induce a range of intracellular polyamine concentrations, and then captured both the polyamine and iron sensor signals on a single-cell basis (Figure 5I-J). Strikingly, we observed a robust inverse relationship between the two reporter readouts (Pearson's correlation coefficient, r, between $(F/F_0)_{iron}$ and $(F/F_0)_{polyamine}$ = -0.91), confirming that polyamine depletion is proportionally coupled to an increase in redox-active iron (Figure 5K). Altogether, these data demonstrate a tight, inverse coupling between polyamine and labile iron levels at the single-cell level, while establishing our genetically encoded reporter as a robust tool for the quantitative dissection of iron biology in living systems.

**Polyamines chelate $Fe^{2+}$ and suppress iron reactivity**

Why does polyamine depletion lead to an increase in redox-active iron? One plausible hypothesis is that polyamines normally buffer intracellular iron through direct coordination. Chemically, polyamines contain multiple amine groups whose nitrogen atoms bear lone electron pairs capable of coordinating vacant orbitals in metal ions, forming stable Werner-type coordination complexes[66]. At physiological pH, polyamines are expected to be predominantly protonated and lack available lone electron pairs for metal coordination[67]. However, in cells, polyamines are extensively complexed with negatively charged

biomolecules, including nucleic acids, ATP, and acidic phospholipids[2]. These electrostatic interactions may shift the local protonation equilibria, partially unmasking nitrogen lone pairs and enabling metal ion coordination[68,69].

We therefore tested whether polyamines can chelate ferrous iron under defined cell-free conditions. We first used FerroOrange as an *in vitro* readout of labile $Fe^{2+}$. FerroOrange fluoresces upon irreversible reaction with $Fe^{2+}$, and reduced signal indicates less $Fe^{2+}$ accessible to the probe[70]. Both spermine and spermidine significantly reduced FerroOrange fluorescence in a concentration-dependent manner (Figure 6A), consistent with polyamine-dependent sequestration of $Fe^{2+}$. As a positive control, the high-affinity iron chelator deferoxamine (DFO) abolished the FerroOrange signal, confirming probe specificity for labile $Fe^{2+}$ (Figure 6A). Notably, increasing the solution pH to 10.5 to favor deprotonation markedly enhanced the $Fe^{2+}$-sequestering activity of both spermidine and spermine (Figure S3H), consistent with an amine-mediated coordination interaction.

In a complementary approach, we performed a ferrozine-based competition assay. Ferrozine forms a chromogenic complex with $Fe^{2+}$ and competition by an alternative chelator would reduce this signal. Addition of spermine decreased ferrozine-$Fe^{2+}$ complex formation in a concentration-dependent manner (Figure 6B). Because ferrozine is a substantially stronger $Fe^{2+}$ chelator, spermine did not fully displace it even at large molar excess (Figure 6B). Nevertheless, the concentration-dependent reduction in signal demonstrates that polyamines can compete with ferrozine for $Fe^{2+}$ binding. In cells, where polyamines are present at millimolar concentrations, even modest per-molecule affinity may translate to substantial overall buffering capacity.

To further establish and characterize polyamine-iron binding, we performed Mössbauer spectroscopy, which provides a direct readout of iron spin states and the local coordination environment[71]. Perturbations in the Fe chemical environment by polyamine binding will be reflected as changes in the isomer shift ($\delta$) and quadrupole splitting ($\Delta E_Q$) parameters, while the extent of binding can be quantified by the relative populations of distinct Fe species. In the presence of polyamines, we observed spectral signatures consistent with formation of a specific $Fe^{2+}$ coordination complex (Figure 6C). Addition of spermine at a 20-fold molar excess relative to $Fe^{2+}$ produced small but reproducible spectral shifts corresponding to ~3% of total iron in spermine-$Fe^{2+}$ complex. Increasing spermine to 60-fold molar

excess further enhanced these shifts, corresponding to ~15% of the total iron in spermine-$Fe^{2+}$ complex, demonstrating concentration-dependent chelation of ferrous iron by spermine. Upon spermine binding, the Mössbauer parameters shifted from those of unbound high-spin $Fe^{2+}$ ($\delta$ = 1.38 mm/s; $\Delta E_Q$ = 3.31 mm/s) to lower values ($\delta$ = 1.34 mm/s, $\Delta E_Q$ = 3.11 mm/s). These changes indicate that $Fe^{2+}$ remains high-spin, while the decreases in $\delta$ and $\Delta E_Q$ reflect increased s-electron density at the nucleus and a more symmetric ligand field, consistent with coordination by a weak-field ligand[72]. These results provide direct evidence for polyamine-$Fe^{2+}$ complex formation and the spectral shifts are consistent with the planar nitrogen-based chelation geometry observed in crystal structures for polyamine-metal complexes[73]. Control ligands (ATP and DFO) produced distinct reference spectra with reduced parameters without altering spin state, further supporting that the observed shifts reflect specific polyamine-dependent $Fe^{2+}$ coordination rather than oxidation or nonspecific perturbation.

Collectively, our data support a model where polyamines act as a physiological buffer for labile iron, stabilizing it in non-reactive complexes and thereby limiting iron-catalyzed lipid peroxidation (Figure 7). Disruption of this buffering system through polyamine depletion liberates this iron, sensitizing cells to ferroptotic death. More broadly, these findings uncover an unexpected layer of iron regulation by polyamines, linking two fundamental metabolic networks with relevance to redox stress, cell death, and disease.

**Discussion**

Our discovery that polyamines regulate iron homeostasis and ferroptosis sensitivity is timely and holds significant implications for numerous ongoing trials investigating polyamine depletion in cancer therapy and other diseases (e.g., NCT06892678 for Ewing sarcoma, NCT05594563 for type 1 diabetes, NCT04301843 for neuroblastoma, NCT04696029 for medulloblastoma, NCT06976424 for hirsutism). An elevated rate of polyamine biosynthesis is a metabolic hallmark of rapid cellular proliferation and growth. This metabolic phenomenon has long been observed in cancer cells and tumors. For example, comparative RNA-seq analyses[74] highlight a striking upregulation of polyamine biosynthesis enzymes (e.g., ODC1, SRM) in tumors compared to paired normal tissues (Figure S4A-B, Table S3). This reprogramming is driven by oncogenic signaling pathways, such as MYC[75], RAS-RAF-MEK[76,77], AKT[78], and mTORC1[79], which converge to sustain polyamine production. Importantly, this metabolic shift is not merely a byproduct of these pathways but are required for the tumorigenic activity of many

of these oncogenes[80,81]. Beyond primary tumor growth, polyamines are also critical for metastatic dissemination[82–86] and immune evasion[87]. While FDA-approved drugs like DFMO, which deplete polyamines, have shown promise in neuroblastoma maintenance therapy[88] and chemoprevention[89], their standalone efficacy against cancer has been limited[90]. Our results identify several novel actionable targets (GPX4, BCL2L1 and ATP13A3), providing a foundation for combination therapies to enhance the efficacy of polyamine depletion in cancer treatment. While this manuscript was under preparation, another study reported that DFMO prevents metastasis in Ewing sarcoma by inducing ferroptosis signatures[91], reinforcing the therapeutic relevance of our findings.

Our discovery that polyamines buffer cellular iron likely reveals an ancient metabolic partnership between two of life's most fundamental molecules. Polyamines and iron emerged early in evolution: polyamines as primordial polycations essential for RNA stability and protein synthesis, iron as the versatile redox cofactor driving cellular chemistry. As early life forms evolved to exploit iron's catalytic power, polyamines were likely co-opted to stabilize redox-active iron and suppress its toxic potential. This dual role of polyamines in supporting macromolecular synthesis while buffering metal-induced damage explains the extraordinary cellular investment in maintaining polyamines at millimolar levels, safeguarded by tightly regulated biosynthetic, catabolism, and transport pathways. By revealing polyamines as redox buffers, our work recasts these elaborate regulatory mechanisms as rapid-response systems for managing cellular iron. This fundamental crosstalk positions polyamine metabolism as a key determinant of ferroptosis sensitivity, with implications spanning bacterial pathogenesis, cold tolerance[92] to cancer therapy.

This conceptual framework is also consistent with clinical and genetic observations linking polyamine metabolism to metal homeostasis. Indeed, polyamines have long been known to coordinate transition metals: early studies demonstrated that neutralized polyamines can form stable complexes with copper, nickel, cobalt, lead, and zinc[93–96]. Structural analysis using X-ray crystallography showed that spermine coordinates copper with its nitrogen donors arranged in a square-planar geometry around the central metal ion[73]. This structure closely resembles the metal-binding architecture observed in other nitrogen-containing biological macrocycles such as porphyrins[97] and is consistent with our Mössbauer spectroscopy showing nitrogen-based coordination in $Fe^{2+}$-spermine complexes. Trientine[98], a tetraamine structurally similar to spermine (Figure S3C), is used therapeutically as a first-line treatment

for copper toxicity in Wilson's disease. It chelates copper, forming stable coordination complexes that are excreted in the urine, thereby lowering systemic copper levels. Notably, patients treated with trientine often exhibit side effects associated with iron deficiency, suggesting that it has broader metal-chelating properties beyond copper[99,100]. On the other hand, polyamine depletion using drugs such as DFMO, frequently causes side effects tied to iron dysregulation, including anemia and thrombocytopenia[101]. Loss of function mutations in ATP13A2, a polyamine transporter linked to early-onset Parkinson's disease, lead to iron accumulation in basal ganglia and cultured dopaminergic neurons[102–105]. Notably, before ATP13A2 was recognized as a polyamine transporter, it was shown to protect cells against broad metal-induced toxicity, including from $Fe^{3+}$, $Mn^{2+}$, and $Zn^{2+}$[106–110]. Similarly, loss-of-function mutations in ATP13A3, the primary polyamine transporter in non-neuronal cells[65], are associated with pulmonary arterial hypertension (PAH)[111], a disease frequently characterized by disruption of iron metabolism[112].

Beyond these genetic disorders, the polyamine-iron axis may also influence age-related physiological decline. Polyamine levels decline with age and this change is traditionally viewed as a passive consequence of reduced biosynthetic activity. Our findings suggest that reduced polyamine levels may result in a progressive failure in iron buffering, contributing to increased oxidative stress and vulnerability to ferroptosis[113]. Notably, recent reports indicate that aged alveolar type 2 (AT2) cells in vivo exhibit elevated labile iron levels compared to young cells, impacting stemness and tumorigenesis[114]. This may be potentially driven, at least in part, by age-related polyamine loss, although requires further investigation.

Conversely, elevated polyamine synthesis in cancer cells might serve a dual purpose: supporting rapid proliferation while simultaneously protecting against oxidative stress arising from dysregulated metabolism. For example, both polyamine[115] and iron metabolism[116–118] are upregulated in cancer stem cells. This metabolic interplay may extend beyond cancer and aging, influencing fundamental processes such as differentiation, immune responses, inflammation, and tissue regeneration, which critically depend on redox control and iron homeostasis. By establishing polyamines as intrinsic iron buffers, we illuminate a previously unrecognized layer of metabolic regulation. Understanding this partnership will be crucial for therapeutic precision, whether exploiting cancer cell dependence on polyamine-mediated iron buffering or protecting healthy tissues from ferroptotic death.

One outstanding question is how polyamines coordinate iron given their predominantly protonated state at physiological pH. Our experiments at alkaline pH demonstrate that deprotonation substantially enhances iron chelation. At intracellular stoichiometries where polyamines exceed labile iron by orders of magnitude, even a small deprotonated fraction could provide substantial buffering capacity. Moreover, polyamines associate extensively with anionic biomolecules (RNA, ATP, phospholipids), which may shift local protonation equilibria and facilitate ternary complex formation. Defining the full repertoire of polyamine-iron species in cells, including their composition, dynamics, and subcellular distribution, remains an important direction for future work.

In addition to iron buffering, polyamine depletion likely perturbs additional pathways that could contribute to ferroptosis sensitivity. Untargeted metabolomics showed that polyamine depletion triggered extensive phospholipid headgroup remodeling, including increased glycerophosphocholine, choline, and phosphoethanolamine (Figure S4D). These metabolites directly feed into phosphatidylcholine and phosphatidylethanolamine synthesis, expanding the pool of oxidizable phospholipid substrates for iron-dependent lipid peroxidation. Consistent with this, lipidomics showed that polyamine depletion, via either genetic or pharmacological interventions, globally increased levels of polyunsaturated phosphatidylcholines and phosphatidylethanolamines, and these changes were reversed by spermidine supplementation (Figure S4E-P). These effects were independent of changes in overall abundance of lipid subtypes (Figure SK-L) or lipid droplet accumulation[119] (Figure S4Q). Because PUFA-containing phospholipids are established ferroptosis substrates[120,121], altered lipid remodeling could act alongside increased labile iron to amplify ferroptotic vulnerability. Mechanistically, this lipid remodeling could reflect altered phospholipase activity: polyamines can be covalently conjugated to phospholipase A2 (PLA2) which regulates its activity[122]. Beyond lipid remodeling, RNA-seq showed that polyamine depletion also suppressed multiple ferroptosis defense genes, including SLC7A11 (cystine import), MTHFD2 and SHMT2 (one-carbon metabolism and NADPH production), and PHGDH and PSAT1 (serine biosynthesis) (Figure S5A-F), suggesting diminished capacity to mount adaptive antioxidant responses. Further work is needed to delineate the relative contributions of lipid processing, iron homeostasis and other pathways to ferroptosis under polyamine-deficient conditions.

An important advance in our work is the development of a genetically encoded fluorescent reporter that enables quantitative measurement of redox-active iron levels in living cells at single-cell resolution. This

reporter leverages the endogenous iron-responsive RNA elements to provide a highly sensitive and dynamic readout of intracellular labile iron concentrations. Unlike chemical probes, which suffer from variable uptake, retention, and clearance, genetically encoded reporters provide stable expression, eliminate loading artifacts, and enable longitudinal tracking of the same cells over time. Its single-cell resolution supports high-throughput screening applications and discovery of novel regulators of iron homeostasis. Furthermore, its ability to track iron dynamics within the same sample opens the door to pharmacokinetic studies of iron-targeting therapies, potentially even in live animal models. We anticipate that this reporter will provide a powerful platform to facilitate future discoveries into iron biology and ferroptosis, advancing our understanding of disease mechanisms and potentially providing novel strategies for therapy development.

**Acknowledgments**

We thank Matthew Vander Heiden, Squire Booker, Catherine Drennan, Elizabeth Nolan, Naama Kanarek, Daniel Suess, and Lindsey Backman for insightful discussions. We thank Punam Bisht for providing MRC-5 fibroblasts, George Bell and Xinlei Gao for assistance with data analysis, and Alex Joseph for support with plasmid preparation. We appreciate valuable feedback from Brighton A. Skeel, Ky Lowenhaupt, Mohamed El-Brolosy, Peter Tsevetkov, Reuben Saunders, Eric Smith, Sarah Willis, Walt Massefski, Mackenzie Field, and the Jain lab. We thank the Whitehead Institute Flow Cytometry Core for assistance with flow cytometry and the MIT Center for Environmental Health Sciences (CEHS) Core, supported by National Institute of Environmental Health Sciences grant P30 ES002109. This work was supported by National Institute of General Medical Sciences (NIGMS) grant R35GM151111 (A.J.), Bumpus Foundation (A.J.), Pew Charitable Trusts (A.J.), Chan Zuckerberg Initiative Collaborative Pairs Award (A.J.), Koch Institute Core Grant P30CA014051 from the National Cancer Institute, the Kathy and Curt Marble Cancer Research Fund, and the Howard Hughes Medical Institute Freeman Hrabowski Scholars Program (W.S.H). S.S. and R.R. acknowledge funding from the Ligue Contre le Cancer (Equipe Labellisée) and Fondation Charles Defforey–Institut de France. J.S. and R.P.M. were supported by National Institute of General Medical Sciences training grant T32GM136540. M.E.P. acknowledges funding from National Institutes of Health grant R35-GM156452

**Contributions**

P.S. designed, performed, analyzed, and interpreted most of the experiments. M.E.P. performed Mossbauer spectroscopy and ferrozine assays. H.R.K. assisted with CRISPR-Cas9 screen. J.S. performed histological analysis and S.I. provided tissue samples. S.M. and I.S.P. helped synthesize reagents with guidance from R.R. and P.T.H., respectively. R.P.M. performed ICP-MS measurements. T.K. and M.W. assisted with metabolomics. C.A. and B.Y. assisted with data analysis. A.D. assisted with lipidomics. L.F. performed the proteomics experiments. A.J. and W.S.H. supervised the project. P.S. wrote the manuscript with edits from A.J. and W.S.H. All authors reviewed and approved the final manuscript.

**Competing interests**

P.S. and A.J. are inventors on a pending patent application based on this work. The remaining authors declare no competing financial interests.

## Figure legends

### Figure 1: CRISPR screen identifies modulators of polyamine sensitivity

(A) Chemical structures of mammalian polyamines.

(B) Schematic of the polyamine metabolic pathway in mammalian cells. DFMO: difluoromethylornithine, Sard: sardomozide.

(C) Cumulative population doublings of K562 cells treated with DFMO (0.5 mM), sardomozide (1 μM), and RO-3306 (5 μM, CDK1 inhibitor) over 12 days. Cells were passaged every 3 days.

(D) Schematic of the CRISPR knockout screen workflow in K562 cells.

(E) Volcano plot showing -log10 (P value) versus median log2 (fold depletion) for all genes identified in the CRISPR drop-out screen. Horizontal line: $p < 0.05$; vertical line: fold change < -1.5. Top hits are highlighted in blue.

(F) Fold change of sgRNAs targeting indicated genes. Each point represents a distinct sgRNA sequence. Error bars indicate mean ± SD (n = 5 sgRNAs).

(G) Viability of AAVS1 and GPX4 knockout (KO) K562 cells treated with sardomozide (5 μM, 96 h).

(H) Viability of K562 cells treated with A-1331852 (0.1 μM, 48 h) following pre-treatment with sardomozide (5 μM, 72 h). DMSO served as the vehicle control.

### Figure 2: Polyamine depletion promotes ferroptosis

(A) Viability of K562 cells treated with ML162 (1 μM, 24 h) or RSL3 (2 μM, 24 h) following pre-treatment with sardomozide (5 μM, 96 h). DMSO served as the vehicle control.

(B) Viability of K562 cells treated with ML162 (1 μM, 24 h) following pre-treatment with sardomozide (5 μM, 72 h) and spermidine (72 h).

(C) Viability of AAVS1, SRM, and SMS knockout (KO) K562 cells treated with ML162 (1 μM, 24 h). SRM KO cells were cultured with spermidine (10 μM) that was removed 6 days before ML162 treatment.

(D) Immunoblot confirming SRM and SMS knockout in K562 cells.

(E) Viability of GPX4 KO K562 cells treated with sardomozide (5 μM, 96 h) plus ferrostatin (2.5 μM), liproxstatin (1 μM) , z-VAD-FMK (15 μM), TTM (10 μM), or GEE (100 μM) for 48 h.

(F) Lipid peroxidation measured using C11-BODIPY (581/591) in K562 cells treated with sardomozide (5 μM, 96 h) and/or ML162 (1 μM, 2.5 h). Data are presented as relative mean fluorescence intensity ± SD (n = 3 biological replicates).

(G-H) Viability of NOMO (G) and HEL (H) cells treated with ML162 (24 h) following pre-treatment with sardomozide (5 μM, 72 h). DMSO served as vehicle control.

**Figure 3: Polyamines act independently of canonical ferroptosis regulators**

(A) Viability of K562 cells treated with ML162 (2 μM, 24 h) following pre-treatment with spermidine (72 h).

(B) Immunoblot showing hypusinated eIF5A levels in K562 cells treated with sardomozide (5 μM, 72 h).

(C) Immunoblot of ACSL4 and GPX4 levels in K562 cells upon sardomozide treatment (5 μM, 96 h).

(D) Immunoblot of FSP1 in K562 cells treated with sardomozide (5 μM, 96 h). OVCAR8 lysate used as a positive control.

(E) Viability of GPX4 KO K562 cells treated with iFSP1 (FSP1 inhibitor) or sardomozide (5 μM, 96 h).

(F) Representative fluorescence of STY-BODIPY oxidation in co-autoxidation assays (2 μM STY-BODIPY, 0.1 mM liposomal soy PC, 200 μM DTUN) with spermidine or PMC (positive control). PMC: 2,2,5,7,8-pentamethyl-6-chromanol.

(G) Viability of K562 cells treated with ML162 (2 μM, 24 h) following pre-treatment with warfarin (50 μM, 3 days) or sardomozide (5 μM, 72 h).

**Figure 4: Polyamine deficiency increases redox-active iron**

(A) Immunoblot of FTH protein in K562 cells treated with sardomozide (5 μM).

(B) Immunoblot of FTH and SRM in SRM KO K562 cells; spermidine (10 μM) was removed 6 days prior to lysate collection.

(C) Immunoblot of FTH in K562 cells treated with sardomozide (5 μM, 48 h) and DFO (50 μM, 48 h).

(D) Viability of K562 cells treated with ML162 (2 μM, 24 h) and DFO (100 μM, 24 h) after pre-treatment with sardomozide (5 μM, 72 h).

(E) Viability of AAVS1 and SRM KO K562 cells treated with ML162 (2 μM, 24 h). SRM KO cells were cultured with spermidine (10 μM) that was removed 8 days before ML162 treatment. DFO (50 μM) was added 24 h prior to ML162.

(F) Viability of AAVS1 and GPX4 KO K562 cells under indicated treatment. FAC (10 mM, 96 h) and liproxstatin (2 μM, 96 h).

(G) Inductively coupled plasma-mass spectrometry (ICP-MS) quantification of cellular iron in K562 cells treated with sardomozide (5 μM, 72 h). FAC (2 mg/mL, 12 h) as positive control.
(H) Immunoblot of FTH in K562 cells in iron-free IMDM treated with sardomozide (5 μM, 48 h). Cells were washed with warm HBSS twice prior to culturing in IMDM.
(I) Relative abundance of indicated metabolites in K562 cells treated with sardomozide (5 μM, 72 h).
(J) Immunoblot of FTH in U-2OS, RPE-1 and MRC-5 cells treated with sardomozide (5 μM, 72 h). DMSO as vehicle control.
(K) Immunoblot of FTH in APC and AKP intestinal organoids treated with sardomozide (5 μM, 48 h). DMSO as vehicle control.
(L) Gene essentiality scores from Cancer Cell Line Encyclopedia for TFRC and AMD1.

**Figure 5: Genetically encoded sensor for redox-active iron**
(A) Schematic of iron-responsive translation initiation of FTH mRNA.
(B) Design of redox-active iron sensor.
(C-D) Representative fluorescence micrographs (C) and flow cytometry quantification (D) of translation initiation efficiency (F = BFP/GFP, $F_0$ = F of control cells) in U-2OS cells expressing iron sensor under indicated treatments. DFO, 100 μM (48 h) and FAC, 10 mM (24 h). Median ± interquartile range from ≥ 100 cells. 50 data points shown. Data: ≥2 independent experiments. Significance via paired two-tailed Student's t-test. Scale bars, 10 μm.

(E) Flow cytometry quantification of translation initiation efficiency (F = BFP/GFP) in K562 cells expressing iron sensor under indicated treatments. DFO, 50 μM (48 h) and FAC, 10 mM (24 h). Median ± interquartile range from ≥ 100 cells. 50 data points shown. Data: ≥2 independent experiments. Significance via Student's t-test.

(F-G) Flow cytometry quantification of translation initiation efficiency (F = BFP/GFP) in (F) U-2OS and (G) K562 cells expressing iron sensor under indicated treatments. Sard, 5 μM (48 h), DFMO 0.5 mM (48 h) and DFO, 100 μM (48 h). Median ± interquartile range from ≥ 100 cells. 50 data points shown. Data: ≥2 independent experiments. Significance via Student's t-test.
(H) Design for the polyamine sensor.
(I) Representative fluorescence micrographs of cells expressing polyamine sensor and iron sensor under indicated treatments. Sard, 5 μM (48 h).

(J) Change in redox-active iron (yellow) and polyamines (purple) measured using respective sensors under sardomozide treatment. Median ± interquartile range from ≥ 100 cells. 50 data points shown.
(K) Linear regression of redox-active iron and polyamine concentration (from Figure 5K).
*** means $p<0.0001$

**Figure 6: Polyamines can chelate metal ions.**
(A) Effect of addition of increasing concentrations of spermidine and spermine on formation of FerroOrange-Fe(II) complex. Experimental conditions: 200 mM HEPES, pH 7.5, 50 μM $FeCl_2$, 1 mM DFO, 10 μM FerroOrange, 5-100 mM spermidine/spermine. DFO used as a positive control.

(B) Effect of addition of increasing concentrations of spermine on formation of ferrozine-Fe(II) complex (562 nm). The fraction of Fe(II) displaced from ferrozine and coordinated by spermine is plotted as a function of spermine concentration. Experimental conditions: 50 mM HEPES, pH 7.5, 200 μM Fe(II).

(C) Effects spermine and other chelators on the $^{57}Fe(II)SO_4$ Mössbauer spectra.

Left, spectra of $^{57}Fe(II)$ in presence of 2 mM DFO (middle), and 2 mM ATP (bottom). In both cases, the spectra are fit as a linear combination of two components: unbound high-spin Fe(II) (green trace) and chelator-bound Fe(II) (DFO-bound, blue trace; ATP-bound, red trace).

Right, effect of increasing concentrations of spermine on the Mössbauer spectrum of $^{57}Fe(II)$. Experimental spectra are shown as black vertical bars. The spectrum of unbound high-spin Fe(II) is fit with a quadrupole doublet with average isomer shift $\delta = 1.38$ mm/s, and quadrupole splitting $\Delta E_Q = 3.31$ mm/s; green trace). In the presence of spermine, the spectra are fit as a mixture of unbound Fe(II) (green trace) and spermine-bound Fe(II) (yellow trace).

All spectra were recorded at 80 K and in zero applied magnetic field. Experimental conditions: [$^{57}Fe(II)$] = 1 mM, 50 mM HEPES, pH 7.5.

**Figure 7: Proposed model for how polyamine depletion increases ferroptotic susceptibility.**
Polyamine depletion frees intracellular $Fe^{2+}$ from polyamine-iron complexes, enhancing redox-active iron pools that drive Fenton chemistry and lipid peroxidation, ultimately causing membrane rupture and ferroptotic cell death.

**Methods**

## RESOURCE AVAILABILITY

### Lead contact

Further information and requests for resources and reagents should be directed to the lead contact, Ankur Jain (ajain@wi.mit.edu) or Whitney Henry (wshenry@mit.edu).

### Materials availability

All unique and stable reagents generated in this study are available from the lead contact upon completion of a Materials Transfer Agreement.

### Data and code availability

CRISPR screen datasets have been deposited in the GEO database under accession number GSE300179. The mapping code for aligning sequence reads to the sgRNA library is accessible via the GitHub repository (https://github.com/whitehead/barc/tree/main/Perl). Additional information required for data reanalysis is available from the lead contact upon request.

### Cell lines and organoids

U-2OS, K562, and RPE1 (immortalized) cell lines were obtained from ATCC. NOMO, HEL, and MEL cells were generously provided by Naama Kanarek (Boston Children's Hospital), and MRC-5 fibroblasts by Punam Bisht (Whitehead Institute). U-2OS, HEK293T, RPE1, and MRC-5 cells were cultured in DMEM (Gibco, Cat# 11965126), while K562, NOMO, HEL, and MEL suspension cells were maintained in RPMI-1640 (Gibco, Cat# 11875093). All media were supplemented with 10% (v/v) fetal bovine serum (FBS; Gibco, Cat# A56707-01, Lot# U2933097RP) and penicillin-streptomycin-glutamine (Gibco, Cat# 10378016). FBS was thawed at 4°C and used without further processing. For iron reporter assays, all cell types were cultured in RPMI supplemented with tetracycline-free cosmic calf serum (CCS) in place of FBS. All cell lines were maintained at 37°C in a humidified atmosphere containing 5% $CO_2$ and were tested monthly for mycoplasma contamination.

### Chemicals

The following reagents were purchased: spermidine trihydrochloride (S2501, Sigma-Aldrich), spermine tetrahydrochloride (J63060.14, Thermo Fisher Scientific), dimethyl sulfoxide (DMSO; 276855, Sigma-Aldrich), DL-α-difluoromethylornithine (DFMO; 16889, Cayman Chemical), iFSP1 (HY-13607, MedChemExpress), warfarin (1719000, Sigma-Aldrich), FerroOrange (F374, Dojindo), BODIPY™ 581/591 C11 (D3861, Thermo Fisher Scientific), liproxstatin-1 (HY-12726, MedChemExpress), RSL3 (HY-100218-A, MedChemExpress), ML162 (HY-100002, MedChemExpress), ferrostatin-1 (Cayman Chemical), Z-VAD(OH)-FAK (Cayman Chemical), STY-BODIPY (Cayman Chemical), PMC (HY-111024, MedChemExpress), A-1331852 (HY-19741, MedChemExpress), iron(II) chloride (220299, Sigma-Aldrich), ferrozine (82950-1G, Sigma-Aldrich), BODIPY 493/503 (MedChemExpress), deferoxamine mesylate (DFO; Cayman Chemical), ferric ammonium citrate (F5879, Sigma), Ellman's reagent (22582, Thermo), oleic acid (O3008, Sigma-Aldrich), and sardomozide dihydrochloride (HY-13746B, MedChemExpress).

**Lentivirus production for CRISPR-Cas9 screen**

$15 \times 10^6$ HEK-293T cells were seeded in T175 $cm^2$ flasks in DMEM (Thermo Fisher Scientific #12430054) supplemented with 10% fetal bovine serum (GeminiBio #100-106). After 24 hours, the media was changed to 20 mL viral production medium: IMDM (Thermo Fisher Scientific #1244053) supplemented with 20% inactivated fetal serum (GeminiBio #100-106). At 32 hours post-seeding, cells were transfected with a mix containing 76.8 µL Xtremegene-9 transfection reagent (Sigma Aldrich #06365779001), 3.62 µg pCMV-VSV-G (Addgene plasmid # 8454)[123], 8.28 µg psPAX2 (a gift from Didier Trono; Addgene plasmid # 12260), and 20 µg sgRNA/Cas9 plasmid and Opti-MEM (Thermo Fisher Scientific #11058021) to a final volume of 1 mL. Media was changed 16 hours later to 55 mL fresh viral production medium. The virus was collected at 48 hours post-transfection and filtered through a 0.45 µm filter, aliquoted, and stored at -80 °C until use.

**CRISPR-Cas9 screen**

A genome-wide lentiviral sgRNA library[26] in a Cas9-containing vector comprising 97,888 unique sgRNA sequences with ~5 sgRNAs per target was used to transduce $390 \times 10^6$ K562 cells to achieve an MOI < 1 (10-20% transduction efficiency) and ~500-1000-fold library coverage. Briefly, polybrene (10 µg/mL final concentration) and virus were mixed with cells ($2.5 \times 10^6$ cells/mL final density) and distributed into individual wells in 6-well plates. Plates were centrifuged at 1126 *g* for 45 minutes at 37 °C and transferred to an incubator. After 8 hours, cells were pelleted, the virus was removed, cells were

resuspended in the fresh growth medium, and transferred to T225 $cm^2$ flasks (250,000 cells/mL final density). After 36 hours, cells were collected and reseeded in fresh growth medium (200,000 cells/mL final density) and puromycin was added (3 µg/mL final concentration). After 3 days, cells were collected and transduction efficiency was determined by comparison of cell survival of transduced cells relative to control cells (untransduced and unselected). Cells were passaged every 2 days ($0.2 \times 10^6$ cells/mL) before DFMO treatment (0.5 mM) starting 9-days post-transduction. At the screen endpoint (14 days DFMO treatment), cell pellets were collected from flasks and frozen at –80 °C.

**Sequencing library preparation**

Genomic DNA (gDNA) was extracted from cell pellets of 20 x $10^6$ cells using the Blood genomicPrep Mini Spin Kit (Cytiva # 28904264) or $60 \times 10^6$ cells using the QIAamp DNA Blood Maxiprep Kit (Qiagen # 51192) according to manufacturer's instructions with minor modifications: Cytiva and QIAGEN Protease were replaced with a 10 mg/mL solution of ProteinaseK (MilliporeSigma # 3115879001) in water; cells were lysed overnight; centrifugation steps after Qiagen Buffer AW1 and AW2 were performed for 2 minutes and 5 minutes, respectively; 2 x 30 µL (Cytiva) or 1 mL (Qiagen) of water preheated to 70 °C was used to elute gDNA (1- or 5-minute incubation), followed by centrifugation for 1 or 5 minutes (Cytiva or Qiagen extractions, respectively). gDNA was quantified using the Qubit dsDNA HS Assay kit (Thermo Fisher Scientific #Q32851).

All PCR reactions were performed in 50 µL reactions using ExTaq Polymerase (Takara Bio #RR001B) using the following primers:

Forward: 5'- AATGATACGGCGACCACCGAGATCTACACCCCACTGACGGGCACCGGA - 3'

Reverse: 5'- CAAGCAGAAGACGGCATACGAGATCnnnnnnTTTCTTGGGTAGTTTGCAGTTTT - 3'

Where "nnnnnn" denotes the barcode used for multiplexing.

For all samples, 1, 3, or 6 µg of gDNA was initially amplified for 28 cycles in 50 µL test PCR reactions. Subsequently, an additional 50 µL reactions were performed using 6 µg per reaction (140 µg gDNA). Reactions were pooled and 100 µL of each sample was purified using HighPrep PCR beads (MagBio Genomics #AC-60005), eluted with 20 µL water, and quantified using the Qubit dsDNA HS Assay kit before sequencing for 26 cycles on an Illumina NovaSeq using the following primers:

Read 1 sequencing primer: 5'-
GTTGATAACGGACTAGCCTTATTTAAACTTGCTATGCTGTTTCCAGCATAGCTCTTAAAC - 3'

Index sequencing primer: 5'-
TTTCAAGTTACGGTAAGCATATGATAGTCCATTTTAAAACATAATTTTAAAACTGCAAACTA
CCCAAGAAA - 3'

**CRISPR screen data analysis**

Sequencing reads were mapped to the sgRNA library using the read_count_CRISPR_guides.pl script available in the GitHub repository (https://github.com/whitehead/barc/tree/main/Perl). The differential sgRNA abundance between DFMO-treated and untreated samples was identified using the Robust Rank Aggregation (RRA) algorithm implemented in the "test" command of MAGeCK (v0.5.9.3)[27].

**Cell viability assays**

K562, NOMO, HEL, and MEL cells were seeded in 6-well plates at defined densities and pre-treated with sardomozide. For 72-hour pre-treatment, $1 \times 10^5$ cells per well were plated in 1 mL of complete growth medium. For extended 96-hour pre-treatment, K562 cells were seeded at $2 \times 10^5$ cells per well in 1 mL of medium and passaged into fresh sardomozide-containing medium after 48 hours. Following completion of the pre-treatment period, cells were transferred to medium supplemented with either ML162 or RSL3 and incubated for an additional 24 to 48 hours prior to downstream viability assessment.

**Lentivirus preparation and transduction**

Lentiviral particles were produced by transient transfection of HEK293T cells with 2 µg of lentiviral transfer plasmid, 1 µg of packaging plasmid psPAX2, and 0.5 µg of envelope plasmid pCMV-VSV-G, using 8 µL of Lipofectamine LTX (Invitrogen, 15338-100) in 500 µL Opti-MEM Reduced Serum Medium (Gibco, 31985-070) according to the manufacturer's instructions. Viral supernatants were harvested 48 hours post-transfection, clarified by filtration through a 0.45-µm filter, and used to transduce target cells in the presence of 10 µg/mL polybrene (Millipore Sigma, TR1003G). Single guide RNA (sgRNA) sequences, Cas9 expression systems, and vector constructs used for CRISPR-Cas9 knockout are detailed in Table S2. Following antibiotic or fluorescence selection, single-cell clones were

isolated, expanded, and validated for gene knockout by immunoblot analysis. Constructs used for the expression of iron and polyamine sensors are also listed in Table S2.

**Western blot**

Cells were washed with ice-cold PBS and lysed in RIPA lysis buffer (25 mM Tris-HCl pH 7.5 (Invitrogen 15567027), 150 mM NaCl (Invitrogen AM9760G), 1% (v/v) NP-40 (Fisher Scientific AAJ19628AP), 1% (w/v) sodium deoxycholate (Sigma-Aldrich D6750), 0.1% (w/v) SDS (Bio-Rad 1610302)) supplemented with 1% (v/v) HALT protease and phosphatase inhibitors (Thermo Scientific 78429) and 125 U/mL Benzonase nuclease (EMD Millipore E1014). Lysates were homogenized and incubated on ice for 30 min with intermittent vortexing every 10 min. Insoluble debris was removed by centrifugation at 21000× g for 10 min at 4°C. Clarified lysates were mixed with 4× Bolt lithium dodecyl sulfate (LDS) sample buffer (Invitrogen B0007) supplemented with 100 mM DTT (Thermo Scientific R0861) and heated at 70°C for 5 min. This boiling step was skipped for membrane proteins (TFRC, FSP1 and SLC40A1) and instead lysate was kept at 37°C for 30 min. Samples were resolved on a Bolt 4-12% Bis-tris polyacrylamide gel (Invitrogen, NW04122) and transferred to PVDF membranes (Invitrogen IB24002) using the iBlot 2 dry blotting system (Invitrogen IB21001).

Membranes were blocked for 1 h at room temperature in 5% (w/v) nonfat dry skim milk (BD Biosciences 232100) prepared in TBST (tris-buffered saline (Fisher Scientific AAJ60764K3) containing 0.1% (v/v) Tween-20 (Fisher Scientific BP337). Primary antibodies were diluted in 5% (w/v) BSA in TBST and incubated overnight at 4°C. After four washes in TBST, membranes were incubated with HRP-conjugated secondary antibodies diluted in 1% (w/v) skim milk in TBST for 1 hour at room temperature. Following four additional TBST washes, chemiluminescent signals were developed using SuperSignal West Femto Maximum Sensitivity Substrate (Thermo Scientific, 34095) and imaged with a ChemiDoc XRS+ system (Bio-Rad). Antibodies were used at the following dilutions: SRM (Proteintech, 19858-1-AP; 1:1000), SMS (Abcam, ab156879; 1:1000), β-actin (Abcam, ab20272; 1:50,000), ACSL4 (Thermo Fisher, PA5-27137; 1:5000), GPX4 (Abcam, ab41787; 1:2000), FSP1 (Cell Signaling Technology, 24972S; 1:1000), Hypusine (Millipore, ABS1064-I; 1:2500), FTH (Abcam, ab75973; 1:2000), TFRC (Invitrogen, 13-6800; 1:5000), SLC40A1 (Novus Biologicals, NBP1-21502; 1:2000), EGFP (Abcam, AB6556; 1:6000), and anti-rabbit HRP-conjugated secondary antibody (Sigma, A0545; 1:5000).

**BODIPY staining**

Cells were pre-treated with sardomozide for 96 h. ML162 was added 2.5 h prior to analysis. 400,000 cells per well were seeded on 6-well dishes for each treatment condition. Cells were incubated with C11-BODIPY (581/591) (5 μM) for 30 min at 37°C. Subsequently, cells were washed once in HBSS (Gibco) and then resuspended in 300 μL of fresh HBSS (Gibco) strained through a 35 μm cell strainer (Falcon tube with cell strainer cap) and analyzed using the FITC and PE-Texas Red filter. At least 10,000 events were analyzed per sample. Data was analyzed using FlowJo Software.

**FENIX assay**

Liposomes were prepared based on methods previously described[36]. Briefly, soy L-α-phosphatidylcholine (PC, Avanti) in chloroform was formed into a thin film using a rotary evaporator (Buchi). The film was hydrated in 3 mL of PBS and sonicated at for 3-5 minutes at 65°C to yield a 20 mM lipid solution. The sample then underwent 3 cycles of freeze-thawing followed by extrusion (Avestin Liposofast LF-50) once at 65°C through a 200 nm membrane (Cytiva Nuclepore) then 3X through 100 nm membranes (Cytiva Nuclepore). The lipid suspension was stored at 4°C. The experiment was performed as previously described[49]. In brief, 0.1 mM liposome was mixed with 2 μM STY-BODIPY (Cayman) and 275 μl of the mixture was added to a black 96-well plate, and compounds (putrescine, spermine or PMC) were added to the indicated concentration, and the samples were incubated for 30 min at 37 °C and initiated by 5 μl of 12 mM DTUN (Cayman) in ethanol, and mixed using pipette to start autoxidation. Data were acquired by STY-BODIPY excitation at 488 nm and emission was measured at 518 nm using a microplate reader.

**RhoNoxM and RhoNox-1 staining**

*RhoNoxM:* Cells were pre-treated with sardomozide (72 h, 5 μM), washed twice with HBSS to remove extracellular iron, resuspended in IMDM, and counted. $0.5 \times 10^6$ cells/well were seeded into 6-well plates with 1 mL iron-free IMDM (Gibco); sardomozide was reintroduced. For iron detection, cells were incubated with RhoNox-M[60] (2 μM, synthesized in-house) for 5 h at 37°C, with ferric ammonium sulfate added during the final hour. Cells were washed three times with pre-warmed HBSS and resuspended in IMDM. For lysosomal content, cells were stained with LysoTracker (20 nM, Thermo Fisher) for 30 min at 37°C in the dark and washed. Flow cytometry was performed using PE (570 nm,

580/14 nm) and APC (638 nm, 660/20 nm) channels. ≥5,000 events/sample were acquired and analyzed using FlowJo.

*RhoNox1:* U-2OS cells were treated with sardomozide (5 μM, 48 h) /and DFO (100 μM, 48 h). Cells were washed three times with pre-warmed HBSS and then incubated with RhoNox-1 (5 μM in IMDM, synthesized in-house) for 4 h at 37°C. Sardomozide and DFO was reintroduced during this incubation. Finally, cells were again washed three times with pre-warmed HBSS and trypsinzed. Flow cytometry was performed using PE (570 nm, 580/14 nm) channel. ≥5,000 events/sample were acquired and analyzed using FlowJo.

**Iron measurements using ICP-MS**

Cells were washed twice with HBSS, counted, and pelleted at $4 \times 10^6$ cells per experimental condition. Cell pellets were snap-frozen in liquid nitrogen and stored briefly at –80°C. For analysis, pellets were thawed and resuspended in 100 μL of trace metal–free water (VWR, 87003-236), transferred to metal-free perfluoroalkoxy (PFA) tubes, and lyophilized overnight. Dried pellets were resuspended in 100 μL of 67% trace metal–free nitric acid (VWR, 87003-226) and digested at 80°C for 20 hours. Digested samples were diluted with trace metal–free water to a final nitric acid concentration of 2%. Blank samples underwent identical processing. An Fe standard curve (0–100,000 ppb; Agilent, 5183-4688) was prepared, and a terbium internal standard (1 ppb final concentration; Agilent, 5190-8590) was added to all samples and standards. Total Fe was quantified using an Agilent 7900 inductively coupled plasma mass spectrometer (ICP-MS) operated with a helium collision cell to minimize polyatomic interferences. Data acquisition and quantification were performed using Agilent MassHunter Workstation software. Sample Fe concentrations were determined by interpolation from the standard curve, blank-subtracted, and normalized to cell number. Statistical analyses were conducted in GraphPad Prism.

**Untargeted metabolomics**

All tubes were pre-chilled, and steps were performed on ice unless otherwise noted. Cells were pelleted by centrifugation at 4°C, washed once with 1.5 mL of ice-cold 0.9% NaCl, and pelleted again to remove the wash solution. Cell pellets were immediately snap-frozen on dry ice. Cells were resuspended in 1 mL of 80% methanol (pre-chilled to 20°C). Tubes were vortexed for 10 minutes in a cold room. Samples were then dried using a SpeedVac concentrator. Dried extracts were stored at –80°C orior to

LC-MS. Polar metabolites were analyzed using a QExactive Orbitrap MS (Thermo) with an Ion Max source and HESI II probe, coupled to a Dionex UltiMate 3000 UHPLC. External calibration was performed weekly. Samples (5 µL) were injected onto a SeQuant ZIC-pHILIC column (2.1 × 150 mm, 5 µm) with a matching guard column. Column and autosampler were maintained at 25°C and 4°C, respectively. Mobile phase A: 20 mM ammonium carbonate, 0.1% ammonium hydroxide; B: acetonitrile. Flow rate: 0.15 mL/min. Gradient: 0–20 min, 80–20% B; 20–20.5 min, 20–80% B; 20.5–28 min, 80% B hold. The MS operated in full-scan, polarity-switching mode (m/z 70–1000), 70,000 resolution, 3.0 kV spray voltage, 275°C capillary, 350°C HESI probe, sheath/aux/sweep gas: 40/15/1. AGC target was $1\times10^6$, max IT 20 ms. For untargeted metabolomics, $ddMS^2$ was acquired on pooled samples (Top 10 method, 15/30/45 V stepped collision energies, 17,500 resolution, AGC $2\times10^5$, max IT 100 ms, isolation window 1.0 m/z). Data were processed in Compound Discoverer 3.1 using an in-house mass list; P-values were Benjamini-Hochberg corrected.

**Thiol metabolomics**

Cysteine and GSH levels (Figure 3G) were measured using a modified Ellman labeling protocol[124]. Briefly, $2 \times 10^6$ cells were pelleted, washed with ice-cold 0.9% NaCl, and extracted with 400 µL ice-cold 80% methanol. Internal standard (10 µL of 4.4 µM 13C,15N-cysteine; HY-Y03375) and 440 µL Ellman's reagent (10 mM in 80% methanol) were added. Samples were incubated on ice for 1 h, centrifuged (3,000 × g, 5 min), and supernatants stored at –80°C until analysis. Samples were run as above with a targeted selected ion monitoring scan (tSIM) in positive mode centred on m/z 319.00530 and m/z 323.01240 to increase signal for the cysteine-TNB (2-nitro-5-thiobenzoic acid) mixed disulfide and the [13C, 15N]cysteine–TNB mixed disulfide, respectively.

**RNA-sequencing**

Total RNA was extracted with PureLink RNA Mini Kit (Invitrogen) per the manufacturer's instruction. PolyA selection and RNA library construction were performed by Novogene with sequencing as 150 × 150 base paired-end libraries using an Illumina NovaSeq 6000 (Novogene), to a depth of ≥ 20M reads. Reads were aligned to the human genome (hg38, annotation file GRCh GTF 38.93) using the short-read alignment tool STAR (version 2.7.1a)[125] with the default options. Expression of each mRNA was calculated and reported as fragments per kilobase of transcript sequence per million base pairs

sequenced (FPKM). The change in FPKM was compared between groups (e.g., control versus sardomozide) and differential expression was analyzed using the DESeq2 package. FDR correction was performed using the Benjamini-Hochberg method.

**Proteomics**

U-2OS cells grown in 6-well plates were harvested at approximately 50% confluency. Culture medium was aspirated, and cells were washed three times with 3 mL PBS. Cells were lysed directly in the wells using 300 µL lysis buffer (50 mM triethylammonium bicarbonate [TEAB], 5% SDS, 2 mM $MgCl_2$) supplemented with benzonase (1 U per mL lysis buffer). Lysates were incubated for 15 min at room temperature with gentle agitation, transferred to low-binding tubes, and clarified by centrifugation at maximum speed for 10 min. The supernatant was transferred to fresh tubes and total protein concentration was determined by BCA assay. Equal amounts of protein (typically 30 µg per sample) were aliquoted, adjusted to equal volumes with lysis buffer, snap-frozen in liquid nitrogen, and stored at −80 °C until submission for mass spectrometry. Sample integrity and loading were verified by SDS-PAGE prior to submission to Whitehead Proteomics Core Facility.

**Microscopy**

Cells were seeded on glass-bottom 96-well plates (Brooks, MGB096-1-2-LG-L) and imaged on a Dragonfly 505 spinning-disk confocal microscope (Andor Technologies) equipped with a piezo Z-stage (ASI) and an iXon Ultra 888 EMCCD camera. Imaging was performed using a 60× oil immersion objective with a pinhole size of 40 µm. Z-stacks were acquired with a step size of 0.3–1 µm, depending on sample thickness (pixel size 121 nm × 121 nm). Cells were maintained at 37 °C and 5% $CO_2$ in a humidified chamber (OKO Labs) during imaging. The following excitation and emission settings were used: YFP (488 nm, 521/38 nm), mCherry (561 nm, 594/43 nm), and miRFP670-2 (637 nm, 620/60 nm). For each condition, at least 40 randomly selected cells were imaged across at least two independent experiments. Representative images were generated as average projections of three z-slices centered on the focal plane.

**Enzymatic polyamine assay**

Measurements were performed using the fluorescent quantification assays (abcam239728) as per the manufacturer's instructions. The polyamine assay buffer (no added polyamine standard) was used as the background.

**C8-pos lipidomics**

Cell pellets ($4 \times 10^6$) were reconstituted in 1 mL isopropanol containing 1,2-didodecanoyl-sn-glycero-3-phosphocholine (Avanti) as internal standard, vortexed, and centrifuged (10,000 × g, 10 min). Supernatants (10 µL) were injected onto a 100 × 2.1 mm, 1.7 µm ACQUITY BEH C8 column (Waters). Lipidomic profiling was performed on a Shimadzu Nexera X2 U-HPLC coupled to an Exactive Plus Orbitrap MS (Thermo), operated in positive ion mode (full scan, m/z 220–1100, 70,000 resolution, 3 Hz acquisition). MS parameters: sheath gas 50, sweep gas 5, in-source CID 5 eV, spray voltage 3 kV, capillary/heater temperatures 300°C, S-lens RF 60, AGC target $1 \times 10^6$, max ion time 100 ms, 1 microscan. The column was eluted with 80% mobile phase A (95:5:0.1, 10 mM ammonium acetate/methanol/formic acid) for 1 min, ramped to 80% mobile phase B (99.9:0.1 methanol/formic acid) over 2 min, then to 100% B over 7 min, and held at 100% B for 3 min. Raw data were processed using TraceFinder software (Thermo Fisher Scientific) for targeted peak integration and manual review of a subset of identified lipids and using Progenesis QI (Nonlinear Dynamics) for peak detection and integration of both lipids of known identify and unknowns. Lipid identities were determined based on comparison to reference plasma extracts and are denoted by total number of carbons in the lipid acyl chain(s) and total number of double bonds in the lipid acyl chain(s).

For lipidomic analysis, only lipid species annotated by Progenesis QI were included; unannotated features were excluded from downstream analysis. To account for differences in total lipid signal arising from variation in sample input or extraction efficiency, the intensity of each annotated lipid species within a sample was normalized to the summed intensity of all annotated lipid species in that sample. Lipid subclass abundances such as O-PC, TG, and others were calculated by summing normalized intensities of species assigned to the same subclass. Within each lipid class such as PC or PE, abundances were further aggregated based on the number of double bonds to assess changes in unsaturation. Because normalization to annotated species can be influenced by incomplete lipid annotation, we additionally analyzed changes at the level of individual lipid species using Z-score normalization across samples. These analyses yielded trends consistent with those observed after abundance normalization, supporting the robustness of the results.

**BODIPY 493/503 lipid droplet measurement**

Cells were pretreated with sardomozide for 72 h and oleic acid for 18 h, then washed twice with HBSS to remove extracellular lipids. Cells ($0.5 \times 10^6$ per well) were seeded into 6-well plates in 1 mL lipid-free IMDM, and sardomozide was reintroduced. Cells were incubated with BODIPY 493/503 (10 μM) for 1 h at 37°C, washed once with HBSS, and resuspended in RPMI 1640 (Gibco). Fluorescence was measured by flow cytometry using the FITC channel (excitation 505 nm, emission 530/30 nm), with at least 5,000 events collected per sample. Data were analyzed using FlowJo.

**Mössbauer spectroscopy**

All samples were prepared in 50 mM HEPES (pH 7.5) under oxygen-free conditions in an anaerobic glovebox (Coylab). Mössbauer spectra were collected using a WEB Research spectrometer (Edina, MN) equipped with a Janis SVT-400 variable-temperature cryostat. Isomer shifts are reported relative to the centroid of an α-iron metal spectrum recorded at room temperature. Spectra were fitted and analyzed using WMOSS software (WEB Research).

**Ferrozine competition assay**

All solutions were prepared in 50 mM HEPES (pH 7.5) under oxygen-free conditions in an anaerobic glovebox (Coylab). $Fe^{2+}$ was supplied as $Fe(II)(NH_4)_2SO_4$ (200 μM). Spermine was added at the indicated concentrations and allowed to equilibrate for 5 min, after which ferrozine was added to a final concentration of 15 μM. Absorbance spectra were recorded using a Cary UV–Vis spectrophotometer (Agilent), and formation of the $Fe^{2+}$–ferrozine complex was monitored at 562 nm.

**FerroOrange assay**

All buffers and salts were prepared aerobically in argon-degassed Milli-Q water and adjusted to the desired pH with NaOH. Spermine and buffer containing FerroOrange were mixed first, and $Fe^{2+}$ was added last to minimize oxidation. Samples were incubated for 30 min in the dark, and fluorescence was measured with excitation at 543 nm and emission at 580 nm.

## References


1. Pegg, A.E. (2016). Functions of Polyamines in Mammals*. J. Biol. Chem. *291*, 14904–14912. https://doi.org/10.1074/jbc.R116.731661.

2. Watanabe, S., Kusama-Eguchi, K., Kobayashi, H., and Igarashi, K. (1991). Estimation of polyamine binding to macromolecules and ATP in bovine lymphocytes and rat liver. J. Biol. Chem. *266*, 20803–20809.

3. Matsufuji, S., Matsufuji, T., Miyazaki, Y., Murakami, Y., Atkins, J.F., Gesteland, R.F., and Hayashi, S. (1995). Autoregulatory frameshifting in decoding mammalian ornithine decarboxylase antizyme. Cell *80*, 51–60. https://doi.org/10.1016/0092-8674(95)90450-6.

4. Rom, E., and Kahana, C. (1994). Polyamines regulate the expression of ornithine decarboxylase antizyme in vitro by inducing ribosomal frame-shifting. Proc. Natl. Acad. Sci. U. S. A. *91*, 3959–3963. https://doi.org/10.1073/pnas.91.9.3959.

5. Pegg, A.E. (2008). Spermidine/spermine-N(1)-acetyltransferase: a key metabolic regulator. Am. J. Physiol. Endocrinol. Metab. *294*, E995-1010. https://doi.org/10.1152/ajpendo.90217.2008.

6. Mitchell, J.L., Judd, G.G., Bareyal-Leyser, A., and Ling, S.Y. (1994). Feedback repression of polyamine transport is mediated by antizyme in mammalian tissue-culture cells. Biochem. J. *299 ( Pt 1)*, 19–22. https://doi.org/10.1042/bj2990019.

7. Park, M.H., and Wolff, E.C. (2018). Hypusine, a polyamine-derived amino acid critical for eukaryotic translation. J. Biol. Chem. *293*, 18710–18718. https://doi.org/10.1074/jbc.TM118.003341.

8. Chattopadhyay, M.K., Park, M.H., and Tabor, H. (2008). Hypusine modification for growth is the major function of spermidine in Saccharomyces cerevisiae polyamine auxotrophs grown in limiting spermidine. Proc. Natl. Acad. Sci. U. S. A. *105*, 6554–6559. https://doi.org/10.1073/pnas.0710970105.

9. Cho, N.H., Cheveralls, K.C., Brunner, A.-D., Kim, K., Michaelis, A.C., Raghavan, P., Kobayashi, H., Savy, L., Li, J.Y., Canaj, H., et al. (2022). OpenCell: Endogenous tagging for the cartography of human cellular organization. Science *375*, eabi6983. https://doi.org/10.1126/science.abi6983.

10. Park, S., Athreya, A., Carrizo, G.E., Benning, N.A., Mitchener, M.M., Bhanu, N.V., Garcia, B.A., Zhang, B., Muir, T.W., Pearce, E.L., et al. (2023). Electrostatic encoding of genome organization principles within single native nucleosomes. BioRxiv Prepr. Serv. Biol., 2023.12.08.570828. https://doi.org/10.1101/2023.12.08.570828.

11. Zhang, D., Zhao, T., Ang, H.S., Chong, P., Saiki, R., Igarashi, K., Yang, H., and Vardy, L.A. (2012). AMD1 is essential for ESC self-renewal and is translationally down-regulated on differentiation to neural precursor cells. Genes Dev. *26*, 461–473. https://doi.org/10.1101/gad.182998.111.

12. Minetti, A., Omrani, O., Brenner, C., Allies, G., Imada, S., Rösler, J., Khawaled, S., Cansiz, F., Meckelmann, S.W., Gebert, N., et al. (2024). Polyamines sustain epithelial regeneration in aged intestines by modulating protein homeostasis. Preprint at bioRxiv, https://doi.org/10.1101/2024.07.26.605278 https://doi.org/10.1101/2024.07.26.605278.

13. Hofer, S.J., Simon, A.K., Bergmann, M., Eisenberg, T., Kroemer, G., and Madeo, F. (2022). Mechanisms of spermidine-induced autophagy and geroprotection. Nat. Aging *2*, 1112–1129. https://doi.org/10.1038/s43587-022-00322-9.

14. Puleston, D.J., Baixauli, F., Sanin, D.E., Edwards-Hicks, J., Villa, M., Kabat, A.M., Kamiński, M.M., Stanckzak, M., Weiss, H.J., Grzes, K.M., et al. (2021). Polyamine metabolism is a central determinant of helper T cell lineage fidelity. Cell *184*, 4186-4202.e20. https://doi.org/10.1016/j.cell.2021.06.007.

15. Gupta, V.K., Scheunemann, L., Eisenberg, T., Mertel, S., Bhukel, A., Koemans, T.S., Kramer, J.M., Liu, K.S.Y., Schroeder, S., Stunnenberg, H.G., et al. (2013). Restoring polyamines protects from age-induced memory impairment in an autophagy-dependent manner. Nat. Neurosci. *16*, 1453–1460. https://doi.org/10.1038/nn.3512.

16. Eisenberg, T., Abdellatif, M., Schroeder, S., Primessnig, U., Stekovic, S., Pendl, T., Harger, A., Schipke, J., Zimmermann, A., Schmidt, A., et al. (2016). Cardioprotection and lifespan extension by the natural polyamine spermidine. Nat. Med. *22*, 1428–1438. https://doi.org/10.1038/nm.4222.

17. Eisenberg, T., Knauer, H., Schauer, A., Büttner, S., Ruckenstuhl, C., Carmona-Gutierrez, D., Ring, J., Schroeder, S., Magnes, C., Antonacci, L., et al. (2009). Induction of autophagy by spermidine promotes longevity. Nat. Cell Biol. *11*, 1305–1314. https://doi.org/10.1038/ncb1975.

18. van Veen, S., Martin, S., Van den Haute, C., Benoy, V., Lyons, J., Vanhoutte, R., Kahler, J.P., Decuypere, J.-P., Gelders, G., Lambie, E., et al. (2020). ATP13A2 deficiency disrupts lysosomal polyamine export. Nature *578*, 419–424. https://doi.org/10.1038/s41586-020-1968-7.

19. Schwartz, C.E., Wang, X., Stevenson, R.E., and Pegg, A.E. (2011). Spermine synthase deficiency resulting in X-linked intellectual disability (Snyder-Robinson syndrome). Methods Mol. Biol. Clifton NJ *720*, 437–445. https://doi.org/10.1007/978-1-61779-034-8_28.

20. Bachmann, A.S., VanSickle, E.A., Michael, J., Vipond, M., and Bupp, C.P. (2024). Bachmann-Bupp syndrome and treatment. Dev. Med. Child Neurol. *66*, 445–455. https://doi.org/10.1111/dmcn.15687.

21. Casero, R.A., Murray Stewart, T., and Pegg, A.E. (2018). Polyamine metabolism and cancer: treatments, challenges and opportunities. Nat. Rev. Cancer *18*, 681–695. https://doi.org/10.1038/s41568-018-0050-3.

22. Shalem, O., Sanjana, N.E., Hartenian, E., Shi, X., Scott, D.A., Mikkelson, T., Heckl, D., Ebert, B.L., Root, D.E., Doench, J.G., et al. (2014). Genome-scale CRISPR-Cas9 knockout screening in human cells. Science *343*, 84–87. https://doi.org/10.1126/science.1247005.

23. Wang, T., Wei, J.J., Sabatini, D.M., and Lander, E.S. (2014). Genetic screens in human cells using the CRISPR-Cas9 system. Science *343*, 80–84. https://doi.org/10.1126/science.1246981.

24. Yang, W.S., SriRamaratnam, R., Welsch, M.E., Shimada, K., Skouta, R., Viswanathan, V.S., Cheah, J.H., Clemons, P.A., Shamji, A.F., Clish, C.B., et al. (2014). Regulation of Ferroptotic Cancer Cell Death by GPX4. Cell *156*, 317–331. https://doi.org/10.1016/j.cell.2013.12.010.

25. Li, Z., Lange, M., Dixon, S.J., and Olzmann, J.A. (2024). Lipid Quality Control and Ferroptosis: From Concept to Mechanism. Annu. Rev. Biochem. *93*, 499–528. https://doi.org/10.1146/annurev-biochem-052521-033527.

26. Inglis, A.J., Guna, A., Gálvez-Merchán, Á., Pal, A., Esantsi, T.K., Keys, H.R., Frenkel, E.M., Oania, R., Weissman, J.S., and Voorhees, R.M. (2023). Coupled protein quality control during nonsense-mediated mRNA decay. J. Cell Sci. *136*, jcs261216. https://doi.org/10.1242/jcs.261216.

27. Li, W., Xu, H., Xiao, T., Cong, L., Love, M.I., Zhang, F., Irizarry, R.A., Liu, J.S., Brown, M., and Liu, X.S. (2014). MAGeCK enables robust identification of essential genes from genome-scale CRISPR/Cas9 knockout screens. Genome Biol. *15*, 554. https://doi.org/10.1186/s13059-014-0554-4.

28. Uemura, T., Yerushalmi, H.F., Tsaprailis, G., Stringer, D.E., Pastorian, K.E., Hawel, L., Byus, C.V., and Gerner, E.W. (2008). Identification and Characterization of a Diamine Exporter in Colon Epithelial Cells. J. Biol. Chem. *283*, 26428–26435. https://doi.org/10.1074/jbc.M804714200.

29. Goldmann, U., and Sedlyarov, V. (2019). RESOLUTE database.

30. Hamouda, N.N., Van den Haute, C., Vanhoutte, R., Sannerud, R., Azfar, M., Mayer, R., Cortés Calabuig, Á., Swinnen, J.V., Agostinis, P., Baekelandt, V., et al. (2021). ATP13A3 is a major component of the enigmatic mammalian polyamine transport system. J. Biol. Chem. *296*, 100182. https://doi.org/10.1074/jbc.RA120.013908.

31. Vander Heiden, M.G., Li, X.X., Gottleib, E., Hill, R.B., Thompson, C.B., and Colombini, M. (2001). Bcl-xL promotes the open configuration of the voltage-dependent anion channel and metabolite passage through the outer mitochondrial membrane. J. Biol. Chem. *276*, 19414–19419. https://doi.org/10.1074/jbc.M101590200.

32. Bi, G., Liang, J., Bian, Y., Shan, G., Huang, Y., Lu, T., Zhang, H., Jin, X., Chen, Z., Zhao, M., et al. (2024). Polyamine-mediated ferroptosis amplification acts as a targetable vulnerability in cancer. Nat. Commun. *15*, 2461. https://doi.org/10.1038/s41467-024-46776-w.

33. Murray Stewart, T., Dunston, T.T., Woster, P.M., and Casero, R.A. (2018). Polyamine catabolism and oxidative damage. J. Biol. Chem. *293*, 18736–18745. https://doi.org/10.1074/jbc.TM118.003337.

34. Zilka, O., Shah, R., Li, B., Friedmann Angeli, J.P., Griesser, M., Conrad, M., and Pratt, D.A. (2017). On the Mechanism of Cytoprotection by Ferrostatin-1 and Liproxstatin-1 and the Role of Lipid Peroxidation in Ferroptotic Cell Death. ACS Cent. Sci. *3*, 232–243. https://doi.org/10.1021/acscentsci.7b00028.

35. Cañeque, T., Baron, L., Müller, S., Carmona, A., Colombeau, L., Versini, A., Solier, S., Gaillet, C., Sindikubwabo, F., Sampaio, J.L., et al. (2025). Activation of lysosomal iron triggers ferroptosis in cancer. Nature *642*, 492–500. https://doi.org/10.1038/s41586-025-08974-4.

36. Li, Y., Ran, Q., Duan, Q., Jin, J., Wang, Y., Yu, L., Wang, C., Zhu, Z., Chen, X., Weng, L., et al. (2024). 7-Dehydrocholesterol dictates ferroptosis sensitivity. Nature *626*, 411–418. https://doi.org/10.1038/s41586-023-06983-9.

37. Tsvetkov, P., Coy, S., Petrova, B., Dreishpoon, M., Verma, A., Abdusamad, M., Rossen, J., Joesch-Cohen, L., Humeidi, R., Spangler, R.D., et al. (2022). Copper induces cell death by targeting lipoylated TCA cycle proteins. Science *375*, 1254–1261. https://doi.org/10.1126/science.abf0529.

38. Alvarez, S.W., Sviderskiy, V.O., Terzi, E.M., Papagiannakopoulos, T., Moreira, A.L., Adams, S., Sabatini, D.M., Birsoy, K., and Possemato, R. (2017). NFS1 undergoes positive selection in lung tumours and protects cells from ferroptosis. Nature *551*, 639–643. https://doi.org/10.1038/nature24637.

39. Tada, K., Nishizawa, H., Shima, H., Muto, A., Wada, M., and Igarashi, K. (2024). Cysteine restriction induces ferroptosis depending on the polyamine biosynthetic pathway in hepatic cancer cells. Preprint at bioRxiv, https://doi.org/10.1101/2024.02.29.582667 https://doi.org/10.1101/2024.02.29.582667.

40. Sanayama, H., Ito, K., Ookawara, S., Uemura, T., Sakiyama, Y., Sugawara, H., Tabei, K., Igarashi, K., and Soda, K. (2023). Whole Blood Spermine/Spermidine Ratio as a New Indicator of Sarcopenia Status in Older Adults. Biomedicines *11*, 1403. https://doi.org/10.3390/biomedicines11051403.

41. Schuller, A.P., Wu, C.C.-C., Dever, T.E., Buskirk, A.R., and Green, R. (2017). eIF5A Functions Globally in Translation Elongation and Termination. Mol. Cell *66*, 194-205.e5. https://doi.org/10.1016/j.molcel.2017.03.003.

42. Manjunath, H., Zhang, H., Rehfeld, F., Han, J., Chang, T.-C., and Mendell, J.T. (2019). Suppression of Ribosomal Pausing by eIF5A Is Necessary to Maintain the Fidelity of Start Codon Selection. Cell Rep. *29*, 3134-3146.e6. https://doi.org/10.1016/j.celrep.2019.10.129.

43. Ray, R.M., Zimmerman, B.J., McCormack, S.A., Patel, T.B., and Johnson, L.R. (1999). Polyamine depletion arrests cell cycle and induces inhibitors p21(Waf1/Cip1), p27(Kip1), and p53 in IEC-6 cells. Am. J. Physiol. *276*, C684-691. https://doi.org/10.1152/ajpcell.1999.276.3.C684.

44. Rodencal, J., Kim, N., He, A., Li, V.L., Lange, M., He, J., Tarangelo, A., Schafer, Z.T., Olzmann, J.A., Long, J.Z., et al. (2024). Sensitization of cancer cells to ferroptosis coincident with cell cycle arrest. Cell Chem. Biol. *31*, 234-248.e13. https://doi.org/10.1016/j.chembiol.2023.10.011.

45. Doll, S., Proneth, B., Tyurina, Y.Y., Panzilius, E., Kobayashi, S., Ingold, I., Irmler, M., Beckers, J., Aichler, M., Walch, A., et al. (2017). ACSL4 dictates ferroptosis sensitivity by shaping cellular lipid composition. Nat. Chem. Biol. *13*, 91–98. https://doi.org/10.1038/nchembio.2239.

46. Doll, S., Freitas, F.P., Shah, R., Aldrovandi, M., da Silva, M.C., Ingold, I., Goya Grocin, A., Xavier da Silva, T.N., Panzilius, E., Scheel, C.H., et al. (2019). FSP1 is a glutathione-independent ferroptosis suppressor. Nature *575*, 693–698. https://doi.org/10.1038/s41586-019-1707-0.

47. Bersuker, K., Hendricks, J.M., Li, Z., Magtanong, L., Ford, B., Tang, P.H., Roberts, M.A., Tong, B., Maimone, T.J., Zoncu, R., et al. (2019). The CoQ oxidoreductase FSP1 acts parallel to GPX4 to inhibit ferroptosis. Nature *575*, 688–692. https://doi.org/10.1038/s41586-019-1705-2.

48. Bellé, N.A.V., Dalmolin, G.D., Fonini, G., Rubin, M.A., and Rocha, J.B.T. (2004). Polyamines reduces lipid peroxidation induced by different pro-oxidant agents. Brain Res. *1008*, 245–251. https://doi.org/10.1016/j.brainres.2004.02.036.

49. Shah, R., Farmer, L.A., Zilka, O., Van Kessel, A.T.M., and Pratt, D.A. (2019). Beyond DPPH: Use of Fluorescence-Enabled Inhibited Autoxidation to Predict Oxidative Cell Death Rescue. Cell Chem. Biol. *26*, 1594-1607.e7. https://doi.org/10.1016/j.chembiol.2019.09.007.

50. Tie, J.-K., Jin, D.-Y., Straight, D.L., and Stafford, D.W. (2011). Functional study of the vitamin K cycle in mammalian cells. Blood *117*, 2967–2974. https://doi.org/10.1182/blood-2010-08-304303.

51. TeSlaa, T., Ralser, M., Fan, J., and Rabinowitz, J.D. (2023). The pentose phosphate pathway in health and disease. Nat. Metab. *5*, 1275–1289. https://doi.org/10.1038/s42255-023-00863-2.

52. Plays, M., Müller, S., and Rodriguez, R. (2021). Chemistry and biology of ferritin. Met. Integr. Biometal Sci. *13*, mfab021. https://doi.org/10.1093/mtomcs/mfab021.

53. Rodriguez, R., Müller, S., Colombeau, L., Solier, S., Sindikubwabo, F., and Cañeque, T. (2025). Metal Ion Signaling in Biomedicine. Chem. Rev. *125*, 660–744. https://doi.org/10.1021/acs.chemrev.4c00577.

54. Galy, B., Conrad, M., and Muckenthaler, M. (2023). Mechanisms controlling cellular and systemic iron homeostasis. Nat. Rev. Mol. Cell Biol., 1–23. https://doi.org/10.1038/s41580-023-00648-1.

55. Brawley, H.N., Kreinbrink, A.C., Hierholzer, J.D., Vali, S.W., and Lindahl, P.A. (2023). Labile Iron Pool of Isolated Escherichia coli Cytosol Likely Includes Fe-ATP and Fe-Citrate but not Fe-Glutathione or Aqueous Fe. J. Am. Chem. Soc. *145*, 2104–2117. https://doi.org/10.1021/jacs.2c06625.

56. Cancer Genome Atlas Network (2012). Comprehensive molecular characterization of human colon and rectal cancer. Nature *487*, 330–337. https://doi.org/10.1038/nature11252.

57. Goto, N., Westcott, P.M.K., Goto, S., Imada, S., Taylor, M.S., Eng, G., Braverman, J., Deshpande, V., Jacks, T., Agudo, J., et al. (2024). SOX17 enables immune evasion of early colorectal adenomas and cancers. Nature *627*, 636–645. https://doi.org/10.1038/s41586-024-07135-3.

58. Tsherniak, A., Vazquez, F., Montgomery, P.G., Weir, B.A., Kryukov, G., Cowley, G.S., Gill, S., Harrington, W.F., Pantel, S., Krill-Burger, J.M., et al. (2017). Defining a Cancer Dependency Map. Cell *170*, 564-576.e16. https://doi.org/10.1016/j.cell.2017.06.010.

59. Hirayama, T., Okuda, K., and Nagasawa, H. (2013). A highly selective turn-on fluorescent probe for iron(II) to visualize labile iron in living cells. Chem. Sci. *4*, 1250–1256. https://doi.org/10.1039/C2SC21649C.

60. Niwa, M., Hirayama, T., Okuda, K., and Nagasawa, H. (2014). A new class of high-contrast Fe(II) selective fluorescent probes based on spirocyclized scaffolds for visualization of intracellular labile iron delivered by transferrin. Org. Biomol. Chem. *12*, 6590–6597. https://doi.org/10.1039/C4OB00935E.

61. Wang, S., Guo, W., Wan, B.-W., Wang, K.-M., Dong, B., Jiang, C.-S., and Zhang, J. (2026). Recent advances in Golgi-targeted fluorescent probes in ferroptosis research. Analyst. https://doi.org/10.1039/D5AN01240F.

62. Hentze, M.W., Muckenthaler, M.U., and Andrews, N.C. (2004). Balancing acts: molecular control of mammalian iron metabolism. Cell *117*, 285–297. https://doi.org/10.1016/s0092-8674(04)00343-5.

63. Eisenstein, R.S., and Blemings, K.P. (1998). Iron regulatory proteins, iron responsive elements and iron homeostasis. J. Nutr. *128*, 2295–2298. https://doi.org/10.1093/jn/128.12.2295.

64. Connell, G.J., Abasiri, I.M., and Chaney, E.H. (2023). A temporal difference in the stabilization of two mRNAs with a 3' iron-responsive element during iron deficiency. RNA N. Y. N *29*, 1117–1125. https://doi.org/10.1261/rna.079665.123.

65. Sharma, P., Kim, C.Y., Keys, H.R., Imada, S., Joseph, A.B., Ferro, L., Kunchok, T., Anderson, R., Yilmaz, O., Weng, J.-K., et al. (2024). Genetically encoded fluorescent reporter for polyamines. BioRxiv Prepr. Serv. Biol., 2024.08.24.609500. https://doi.org/10.1101/2024.08.24.609500.

66. Ueda, H., Suzuki, M., Kuroda, R., Tanaka, T., and Aoki, S. (2021). Design, Synthesis, and Biological Evaluation of Boron-Containing Macrocyclic Polyamines and Their Zinc(II) Complexes for Boron Neutron Capture Therapy. J. Med. Chem. *64*, 8523–8544. https://doi.org/10.1021/acs.jmedchem.1c00445.

67. 24.3: Basicity of Amines (2015). Chem. Libr. https://chem.libretexts.org/Bookshelves/Organic_Chemistry/Organic_Chemistry_(Morsch_et_al.)/24%3A_Amines_and_Heterocycles/24.03%3A_Basicity_of_Amines.

68. Kontoghiorghes, G.J., and Kontoghiorghe, C.N. (2020). Iron and Chelation in Biochemistry and Medicine: New Approaches to Controlling Iron Metabolism and Treating Related Diseases. Cells *9*, 1456. https://doi.org/10.3390/cells9061456.

69. Zhang, Y., Zhao, X., Qin, Y., Li, X., Chang, Y., Shi, Z., Song, M., Sun, W., Xiao, J., Li, Z., et al. (2023). Order-order assembly transition-driven polyamines detection based on iron-sulfur complexes. Commun. Chem. *6*, 146. https://doi.org/10.1038/s42004-023-00942-1.

70. Grubwieser, P., Brigo, N., Seifert, M., Grander, M., Theurl, I., Nairz, M., Weiss, G., and Pfeifhofer-Obermair, C. (2024). Quantification of Macrophage Cellular Ferrous Iron (Fe2+) Content Using a

Highly Specific Fluorescent Probe in a Plate Reader. Bio-Protoc. *14*, e4929. https://doi.org/10.21769/BioProtoc.4929.

71. Gütlich, P., Bill, E., and Trautwein, A.X. (2010). Mössbauer Spectroscopy and Transition Metal Chemistry: Fundamentals and Applications (Springer Science & Business Media).

72. Greenwood, N.N. (2012). Mössbauer Spectroscopy (Springer Science & Business Media).

73. Boggs, R., and Donohue, J. (1975). Spermine copper(II) perchlorate. Acta Crystallogr. B *31*, 320–322. https://doi.org/10.1107/S0567740875002658.

74. Tang, Z., Li, C., Kang, B., Gao, G., Li, C., and Zhang, Z. (2017). GEPIA: a web server for cancer and normal gene expression profiling and interactive analyses. Nucleic Acids Res. *45*, W98–W102. https://doi.org/10.1093/nar/gkx247.

75. Bello-Fernandez, C., Packham, G., and Cleveland, J.L. (1993). The ornithine decarboxylase gene is a transcriptional target of c-Myc. Proc. Natl. Acad. Sci. U. S. A. *90*, 7804–7808. https://doi.org/10.1073/pnas.90.16.7804.

76. Origanti, S., and Shantz, L.M. (2007). Ras transformation of RIE-1 cells activates cap-independent translation of ornithine decarboxylase: regulation by the Raf/MEK/ERK and phosphatidylinositol 3-kinase pathways. Cancer Res. *67*, 4834–4842. https://doi.org/10.1158/0008-5472.CAN-06-4627.

77. Roy, U.K.B., Rial, N.S., Kachel, K.L., and Gerner, E.W. (2008). Activated K-RAS increases polyamine uptake in human colon cancer cells through modulation of caveolar endocytosis. Mol. Carcinog. *47*, 538–553. https://doi.org/10.1002/mc.20414.

78. Kucharzewska, P., Welch, J.E., Svensson, K.J., and Belting, M. (2009). The polyamines regulate endothelial cell survival during hypoxic stress through PI3K/AKT and MCL-1. Biochem. Biophys. Res. Commun. *380*, 413–418. https://doi.org/10.1016/j.bbrc.2009.01.097.

79. Zabala-Letona, A., Arruabarrena-Aristorena, A., Martín-Martín, N., Fernandez-Ruiz, S., Sutherland, J.D., Clasquin, M., Tomas-Cortazar, J., Jimenez, J., Torres, I., Quang, P., et al. (2017). mTORC1-dependent AMD1 regulation sustains polyamine metabolism in prostate cancer. Nature *547*, 109–113. https://doi.org/10.1038/nature22964.

80. Hogarty, M.D., Norris, M.D., Davis, K., Liu, X., Evageliou, N.F., Hayes, C.S., Pawel, B., Guo, R., Zhao, H., Sekyere, E., et al. (2008). ODC1 is a critical determinant of MYCN oncogenesis and a therapeutic target in neuroblastoma. Cancer Res. *68*, 9735–9745. https://doi.org/10.1158/0008-5472.CAN-07-6866.

81. Rounbehler, R.J., Li, W., Hall, M.A., Yang, C., Fallahi, M., and Cleveland, J.L. (2009). Targeting ornithine decarboxylase impairs development of MYCN-amplified neuroblastoma. Cancer Res. *69*, 547–553. https://doi.org/10.1158/0008-5472.CAN-08-2968.

82. Manni, A., Washington, S., Hu, X., Griffith, J.W., Bruggeman, R., Demers, L.M., Mauger, D., and Verderame, M.F. (2005). Effects of polyamine synthesis inhibitors on primary tumor features and

metastatic capacity of human breast cancer cells. Clin. Exp. Metastasis *22*, 255–263. https://doi.org/10.1007/s10585-005-8480-1.

83. Klein, S., Miret, J.J., Algranati, I.D., and de Lustig, E.S. (1985). Effect of alpha-difluoromethylornithine in lung metastases before and after surgery of primary adenocarcinoma tumors in mice. Biol. Cell *53*, 33–36. https://doi.org/10.1111/j.1768-322x.1985.tb00352.x.

84. Herr, H.W., Kleinert, E.L., Conti, P.S., Burchenal, J.H., and Whitmore, W.F. (1984). Effects of alpha-difluoromethylornithine and methylglyoxal bis(guanylhydrazone) on the growth of experimental renal adenocarcinoma in mice. Cancer Res. *44*, 4382–4385.

85. Kubota, S., Ohsawa, N., and Takaku, F. (1987). Effects of DL-alpha-difluoromethylornithine on the growth and metastasis of B16 melanoma in vivo. Int. J. Cancer *39*, 244–247. https://doi.org/10.1002/ijc.2910390220.

86. Kubota, S., Kiyosawa, H., Nomura, Y., Yamada, T., and Seyama, Y. (1997). Ornithine decarboxylase overexpression in mouse 10T1/2 fibroblasts: cellular transformation and invasion. J. Natl. Cancer Inst. *89*, 567–571. https://doi.org/10.1093/jnci/89.8.567.

87. Hibino, S., Eto, S., Hangai, S., Endo, K., Ashitani, S., Sugaya, M., Osawa, T., Soga, T., Taniguchi, T., and Yanai, H. (2023). Tumor cell-derived spermidine is an oncometabolite that suppresses TCR clustering for intratumoral CD8+ T cell activation. Proc. Natl. Acad. Sci. U. S. A. *120*, e2305245120. https://doi.org/10.1073/pnas.2305245120.

88. Sholler, G.L.S., Ferguson, W., Bergendahl, G., Bond, J.P., Neville, K., Eslin, D., Brown, V., Roberts, W., Wada, R.K., Oesterheld, J., et al. (2018). Maintenance DFMO Increases Survival in High Risk Neuroblastoma. Sci. Rep. *8*, 14445. https://doi.org/10.1038/s41598-018-32659-w.

89. Simoneau, A.R., Gerner, E.W., Nagle, R., Ziogas, A., Fujikawa-Brooks, S., Yerushalmi, H., Ahlering, T.E., Lieberman, R., McLaren, C.E., Anton-Culver, H., et al. (2008). The Effect of Difluoromethylornithine on Decreasing Prostate Size and Polyamines in Men: Results of a Year-Long Phase IIb Randomized Placebo-Controlled Chemoprevention Trial. Cancer Epidemiol. Biomark. Prev. Publ. Am. Assoc. Cancer Res. Cosponsored Am. Soc. Prev. Oncol. *17*, 292–299. https://doi.org/10.1158/1055-9965.EPI-07-0658.

90. Holbert, C.E., Cullen, M.T., Casero, R.A., and Stewart, T.M. (2022). Polyamines in cancer: integrating organismal metabolism and antitumour immunity. Nat. Rev. Cancer *22*, 467–480. https://doi.org/10.1038/s41568-022-00473-2.

91. Offenbacher, R., Jackson, K.W., Hayashi, M., Zhang, J., Peng, D., Tan, Y., Stewart, T.M., Ciero, P., Foley, J., Casero, R.A., et al. (2024). Polyamine Depletion by D, L-alpha-difluoromethylornithine Inhibits Ewing Sarcoma Metastasis by Inducing Ferroptosis. BioRxiv Prepr. Serv. Biol., 2024.06.14.599064. https://doi.org/10.1101/2024.06.14.599064.

92. Lam, B., Kajderowicz, K.M., Keys, H.R., Roessler, J.M., Frenkel, E.M., Kirkland, A., Bisht, P., El-Brolosy, M.A., Jaenisch, R., Bell, G.W., et al. (2024). Multi-species genome-wide CRISPR screens identify conserved suppressors of cold-induced cell death. BioRxiv Prepr. Serv. Biol., 2024.07.25.605098. https://doi.org/10.1101/2024.07.25.605098.

93. Hares, G.B., Fernelius, W.C., and Douglas, B.E. (1956). Equilibrium Constants for the Formation of Complexes between Metal Ions and Polyamines1,2. J. Am. Chem. Soc. *78*, 1816–1818. https://doi.org/10.1021/ja01590a011.

94. Bertsch, C.R., Fernelius, W.C., and Block, B.P. (1958). A Thermodynamic Study of Some Complexes of Metal Ions with Polyamines. J. Phys. Chem. *62*, 444–450. https://doi.org/10.1021/j150562a018.

95. Palmer, B.N., and Powell, H.K.J. (1974). Complex formation between 4,9-diazadodecane-1,12-diamine (spermine) and copper(II) ions and protons in aqueous solution. J. Chem. Soc. Dalton Trans., 2086–2089. https://doi.org/10.1039/DT9740002086.

96. Barbucci, R., Campbell, M.J.M., Cannas, M., and Marongiu, G. (1980). Seven membered chelate rings in copper(II) complexes with spermidine. Inorganica Chim. Acta *46*, 135–138. https://doi.org/10.1016/S0020-1693(00)84181-X.

97. LØVaas, E. (1996). Antioxidative and Metal-Chelating Effects of Polyamines11Dedicated to the memory of David E. Green: Long gone but not forgotten. In Advances in Pharmacology, H. Sies, ed. (Academic Press), pp. 119–149. https://doi.org/10.1016/S1054-3589(08)60982-5.

98. Kamlin, C.O.F., M. Jenkins, T., L Heise, J., and S. Amin, N. (2024). Trientine Tetrahydrochloride, From Bench to Bedside: A Narrative Review. Drugs *84*, 1509–1518. https://doi.org/10.1007/s40265-024-02099-0.

99. Roberts, E.A., Schilsky, M.L., and American Association for Study of Liver Diseases (AASLD) (2008). Diagnosis and treatment of Wilson disease: an update. Hepatol. Baltim. Md *47*, 2089–2111. https://doi.org/10.1002/hep.22261.

100. Perry, A.R., Pagliuca, A., Fitzsimons, E.J., Mufti, G.J., and Williams, R. (1996). Acquired sideroblastic anaemia induced by a copper-chelating agent. Int. J. Hematol. *64*, 69–72. https://doi.org/10.1016/0925-5710(96)00457-4.

101. Tangella, A.V., Gajre, A.S., Chirumamilla, P.C., and Rathhan, P.V. Difluoromethylornithine (DFMO) and Neuroblastoma: A Review. Cureus *15*, e37680. https://doi.org/10.7759/cureus.37680.

102. Ramirez, A., Heimbach, A., Gründemann, J., Stiller, B., Hampshire, D., Cid, L.P., Goebel, I., Mubaidin, A.F., Wriekat, A.-L., Roeper, J., et al. (2006). Hereditary parkinsonism with dementia is caused by mutations in ATP13A2, encoding a lysosomal type 5 P-type ATPase. Nat. Genet. *38*, 1184–1191. https://doi.org/10.1038/ng1884.

103. Kırımtay, K., Temizci, B., Gültekin, M., Yapıcı, Z., and Karabay, A. (2021). Novel mutations in ATP13A2 associated with mixed neurological presentations and iron toxicity due to nonsense-mediated decay. Brain Res. *1750*, 147167. https://doi.org/10.1016/j.brainres.2020.147167.

104. Schneider, S.A., Paisan-Ruiz, C., Quinn, N.P., Lees, A.J., Houlden, H., Hardy, J., and Bhatia, K.P. (2010). ATP13A2 mutations (PARK9) cause neurodegeneration with brain iron accumulation. Mov. Disord. *25*, 979–984. https://doi.org/10.1002/mds.22947.

105. Rajagopalan, S., Rane, A., Chinta, S.J., and Andersen, J.K. (2016). Regulation of ATP13A2 via PHD2-HIF1α Signaling Is Critical for Cellular Iron Homeostasis: Implications for Parkinson's Disease. J. Neurosci. Off. J. Soc. Neurosci. *36*, 1086–1095. https://doi.org/10.1523/JNEUROSCI.3117-15.2016.

106. Gitler, A.D., Chesi, A., Geddie, M.L., Strathearn, K.E., Hamamichi, S., Hill, K.J., Caldwell, K.A., Caldwell, G.A., Cooper, A.A., Rochet, J.-C., et al. (2009). Alpha-synuclein is part of a diverse and highly conserved interaction network that includes PARK9 and manganese toxicity. Nat. Genet. *41*, 308–315. https://doi.org/10.1038/ng.300.

107. Schmidt, K., Wolfe, D.M., Stiller, B., and Pearce, D.A. (2009). Cd2+, Mn2+, Ni2+ and Se2+ toxicity to *Saccharomyces cerevisiae* lacking YPK9p the orthologue of human ATP13A2. Biochem. Biophys. Res. Commun. *383*, 198–202. https://doi.org/10.1016/j.bbrc.2009.03.151.

108. Kong, S.M.Y., Chan, B.K.K., Park, J.-S., Hill, K.J., Aitken, J.B., Cottle, L., Farghaian, H., Cole, A.R., Lay, P.A., Sue, C.M., et al. (2014). Parkinson's disease-linked human PARK9/ATP13A2 maintains zinc homeostasis and promotes α-Synuclein externalization via exosomes. Hum. Mol. Genet. *23*, 2816–2833. https://doi.org/10.1093/hmg/ddu099.

109. Rinaldi, D.E., Corradi, G.R., Cuesta, L.M., Adamo, H.P., and de Tezanos Pinto, F. (2015). The Parkinson-associated human P5B-ATPase ATP13A2 protects against the iron-induced cytotoxicity. Biochim. Biophys. Acta *1848*, 1646–1655. https://doi.org/10.1016/j.bbamem.2015.04.008.

110. Martin, S., van Veen, S., Holemans, T., Demirsoy, S., van den Haute, C., Baekelandt, V., Agostinis, P., Eggermont, J., and Vangheluwe, P. (2016). Protection against Mitochondrial and Metal Toxicity Depends on Functional Lipid Binding Sites in ATP13A2. Park. Dis. *2016*, e9531917. https://doi.org/10.1155/2016/9531917.

111. Liu, B., Azfar, M., Legchenko, E., West, J.A., Martin, S., Van den Haute, C., Baekelandt, V., Wharton, J., Howard, L., Wilkins, M.R., et al. (2024). ATP13A3 variants promote pulmonary arterial hypertension by disrupting polyamine transport. Cardiovasc. Res. *120*, 756–768. https://doi.org/10.1093/cvr/cvae068.

112. Soon, E., Treacy, C.M., Toshner, M.R., MacKenzie-Ross, R., Manglam, V., Busbridge, M., Sinclair-McGarvie, M., Arnold, J., Sheares, K.K., Morrell, N.W., et al. (2011). Unexplained iron deficiency in idiopathic and heritable pulmonary arterial hypertension. Thorax *66*, 326–332. https://doi.org/10.1136/thx.2010.147272.

113. Mazhar, M., Din, A.U., Ali, H., Yang, G., Ren, W., Wang, L., Fan, X., and Yang, S. (2021). Implication of ferroptosis in aging. Cell Death Discov. *7*, 149. https://doi.org/10.1038/s41420-021-00553-6.

114. Zhuang, X., Wang, Q., Joost, S., Ferrena, A., Humphreys, D.T., Li, Z., Blum, M., Krause, K., Ding, S., Landais, Y., et al. (2025). Ageing limits stemness and tumorigenesis by reprogramming iron homeostasis. Nature *637*, 184–194. https://doi.org/10.1038/s41586-024-08285-0.

115. Tamari, K., Konno, M., Asai, A., Koseki, J., Hayashi, K., Kawamoto, K., Murai, N., Matsufuji, S., Isohashi, F., Satoh, T., et al. (2018). Polyamine flux suppresses histone lysine demethylases and

enhances ID1 expression in cancer stem cells. Cell Death Discov. *4*, 104. https://doi.org/10.1038/s41420-018-0117-7.

116. Müller, S., Sindikubwabo, F., Cañeque, T., Lafon, A., Versini, A., Lombard, B., Loew, D., Wu, T.-D., Ginestier, C., Charafe-Jauffret, E., et al. (2020). CD44 regulates epigenetic plasticity by mediating iron endocytosis. Nat. Chem. *12*, 929–938. https://doi.org/10.1038/s41557-020-0513-5.

117. Mai, T.T., Hamaï, A., Hienzsch, A., Cañeque, T., Müller, S., Wicinski, J., Cabaud, O., Leroy, C., David, A., Acevedo, V., et al. (2017). Salinomycin kills cancer stem cells by sequestering iron in lysosomes. Nat. Chem. *9*, 1025–1033. https://doi.org/10.1038/nchem.2778.

118. Schonberg, D.L., Miller, T.E., Wu, Q., Flavahan, W.A., Das, N.K., Hale, J.S., Hubert, C.G., Mack, S.C., Jarrar, A.M., Karl, R.T., et al. (2015). Preferential Iron Trafficking Characterizes Glioblastoma Stem-like Cells. Cancer Cell *28*, 441–455. https://doi.org/10.1016/j.ccell.2015.09.002.

119. Cruz-Pulido, Y.E., LoMascolo, N.J., May, D., Hatahet, J., Thomas, C.E., Chu, A.K.W., Stacey, S.P., Villanueva Guzman, M. del M., Aubert, G., and Mounce, B.C. (2024). Polyamines mediate cellular energetics and lipid metabolism through mitochondrial respiration to facilitate virus replication. PLOS Pathog. *20*, e1012711. https://doi.org/10.1371/journal.ppat.1012711.

120. Zou, Y., Henry, W.S., Ricq, E.L., Graham, E.T., Phadnis, V.V., Maretich, P., Paradkar, S., Boehnke, N., Deik, A.A., Reinhardt, F., et al. (2020). Plasticity of ether lipids promotes ferroptosis susceptibility and evasion. Nature *585*, 603–608. https://doi.org/10.1038/s41586-020-2732-8.

121. Dixon, S.J., and Olzmann, J.A. (2024). The cell biology of ferroptosis. Nat. Rev. Mol. Cell Biol. *25*, 424–442. https://doi.org/10.1038/s41580-024-00703-5.

122. Cordella-Miele, E., Miele, L., Beninati, S., and Mukherjee, A.B. (1993). Transglutaminase-catalyzed incorporation of polyamines into phospholipase A2. J. Biochem. (Tokyo) *113*, 164–173. https://doi.org/10.1093/oxfordjournals.jbchem.a124021.

123. Stewart, S.A., Dykxhoorn, D.M., Palliser, D., Mizuno, H., Yu, E.Y., An, D.S., Sabatini, D.M., Chen, I.S.Y., Hahn, W.C., Sharp, P.A., et al. (2003). Lentivirus-delivered stable gene silencing by RNAi in primary cells. RNA N. Y. N *9*, 493–501. https://doi.org/10.1261/rna.2192803.

124. Adelmann, C.H., Traunbauer, A.K., Chen, B., Condon, K.J., Chan, S.H., Kunchok, T., Lewis, C.A., and Sabatini, D.M. (2020). MFSD12 mediates the import of cysteine into melanosomes and lysosomes. Nature *588*, 699–704. https://doi.org/10.1038/s41586-020-2937-x.

125. Dobin, A., Davis, C.A., Schlesinger, F., Drenkow, J., Zaleski, C., Jha, S., Batut, P., Chaisson, M., and Gingeras, T.R. (2013). STAR: ultrafast universal RNA-seq aligner. Bioinforma. Oxf. Engl. *29*, 15–21. https://doi.org/10.1093/bioinformatics/bts635.

# Figure 1: CRISPR screen reveals modulators of polyamine sensitivty

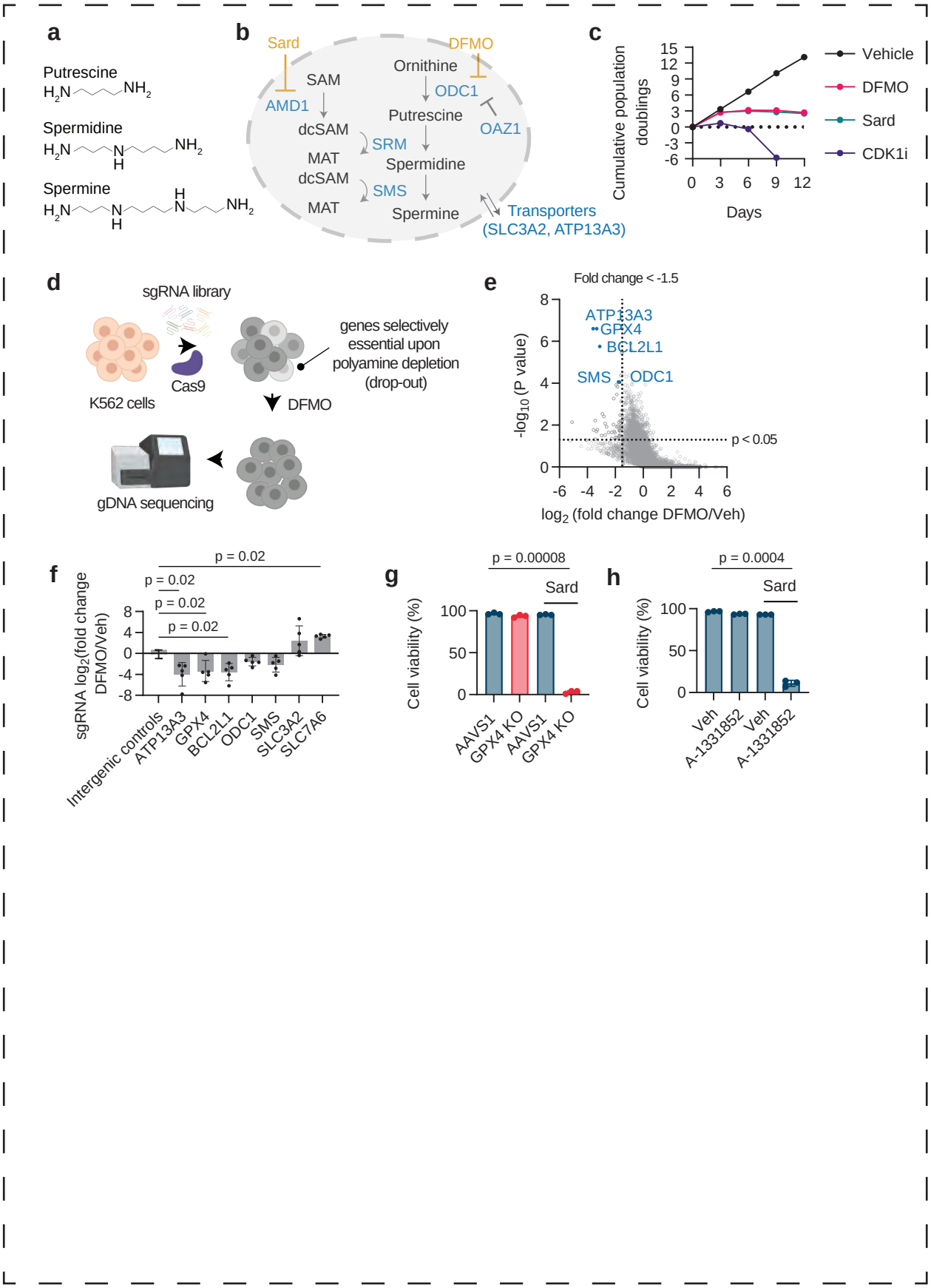

Figure 2: Polyamine depletion promotes ferroptosis

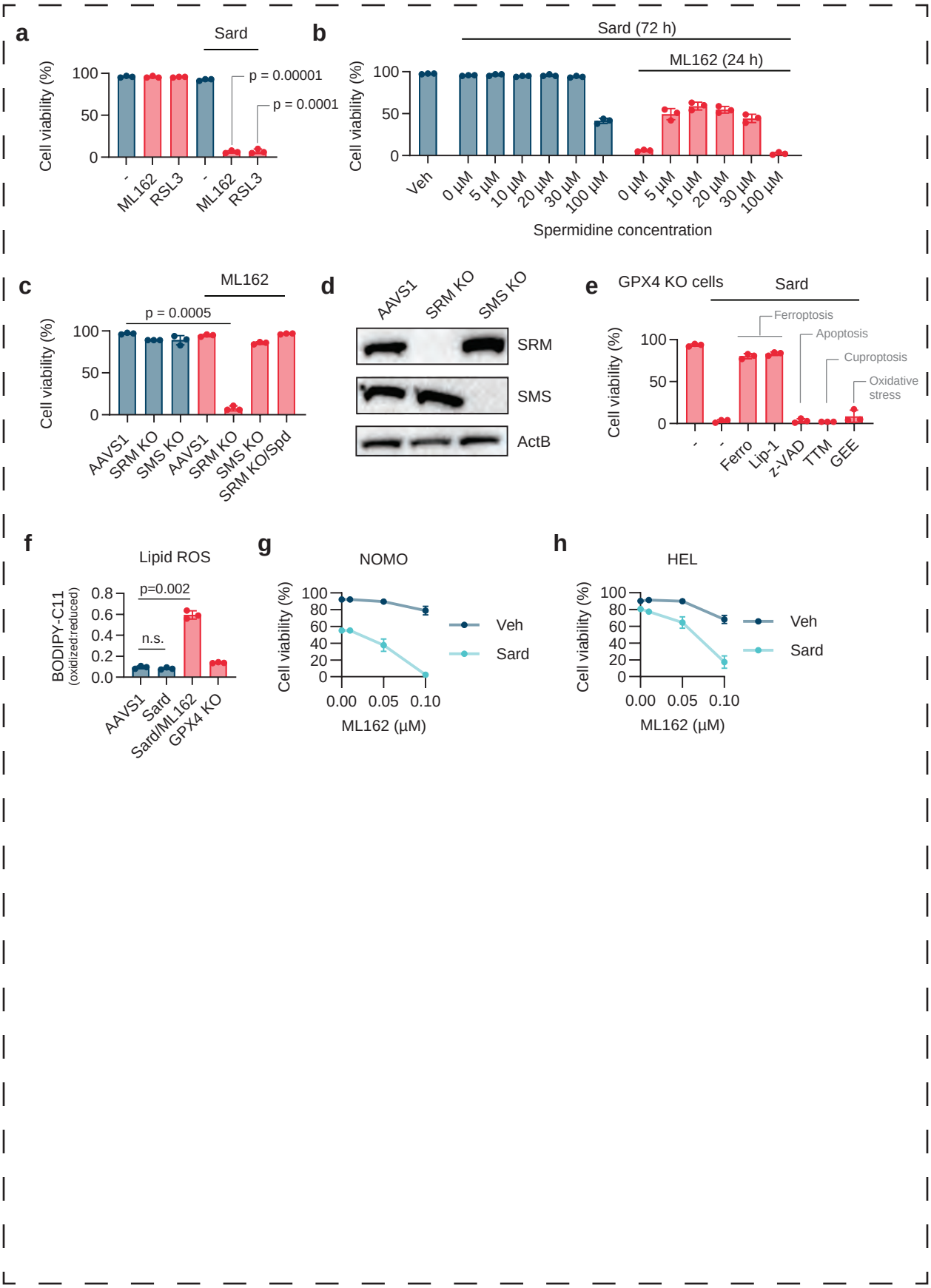

Figure 3: Polyamines act independently of major ferroptosis regulators

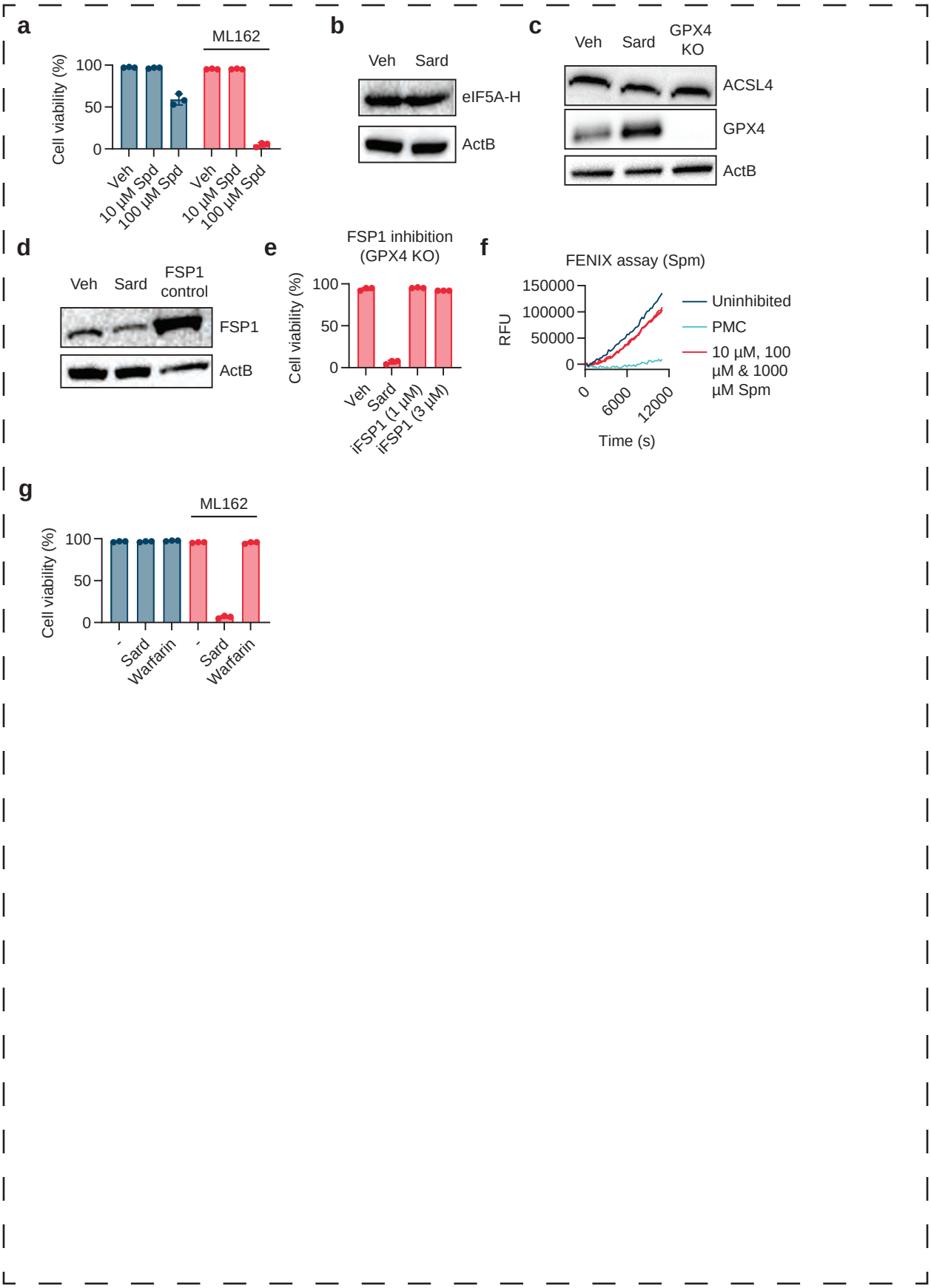

# Figure 4: Polyamine deficiency increases redox-active iron

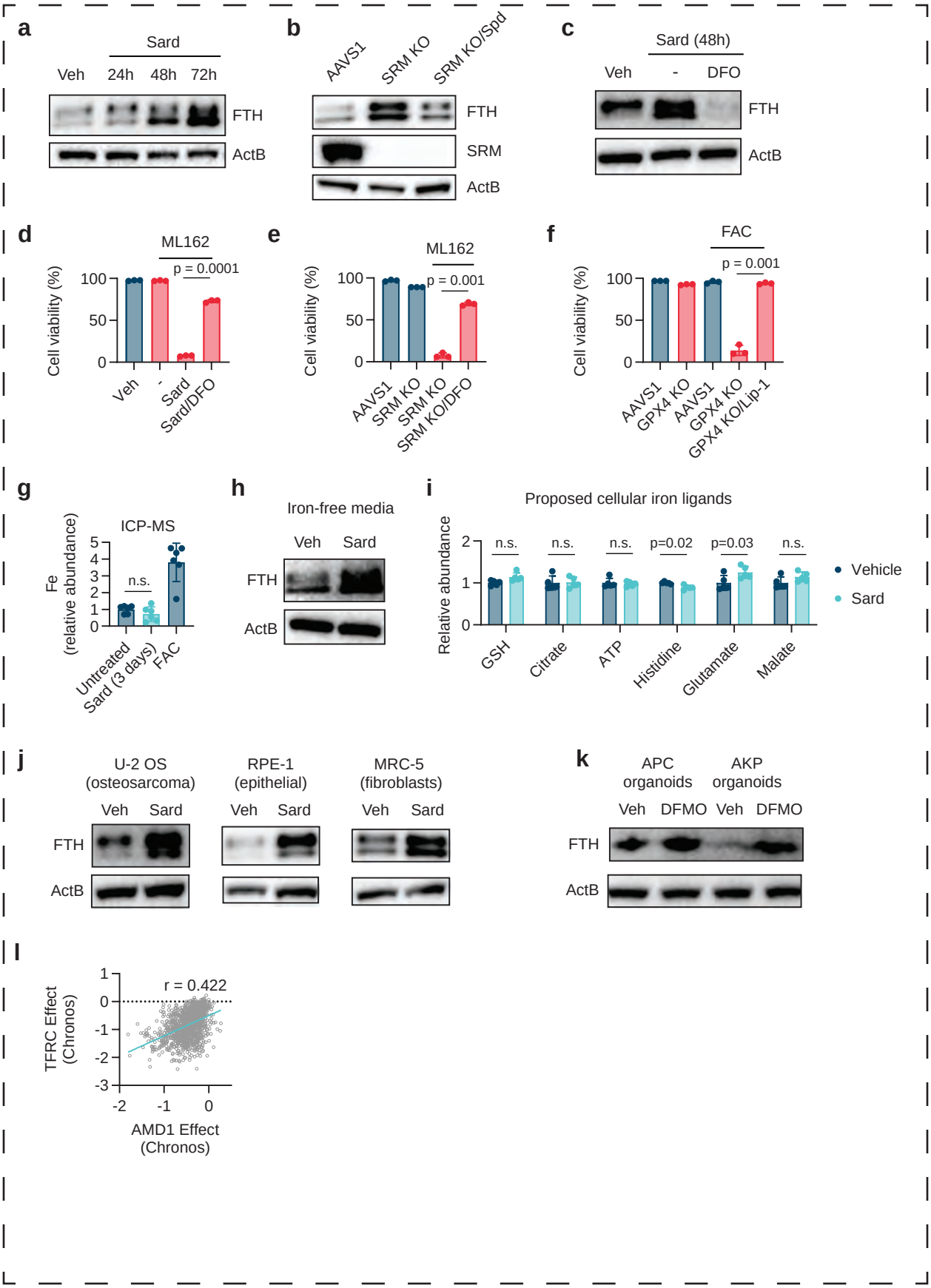

# Figure 5: Genetically encoded sensor for redox-active iron

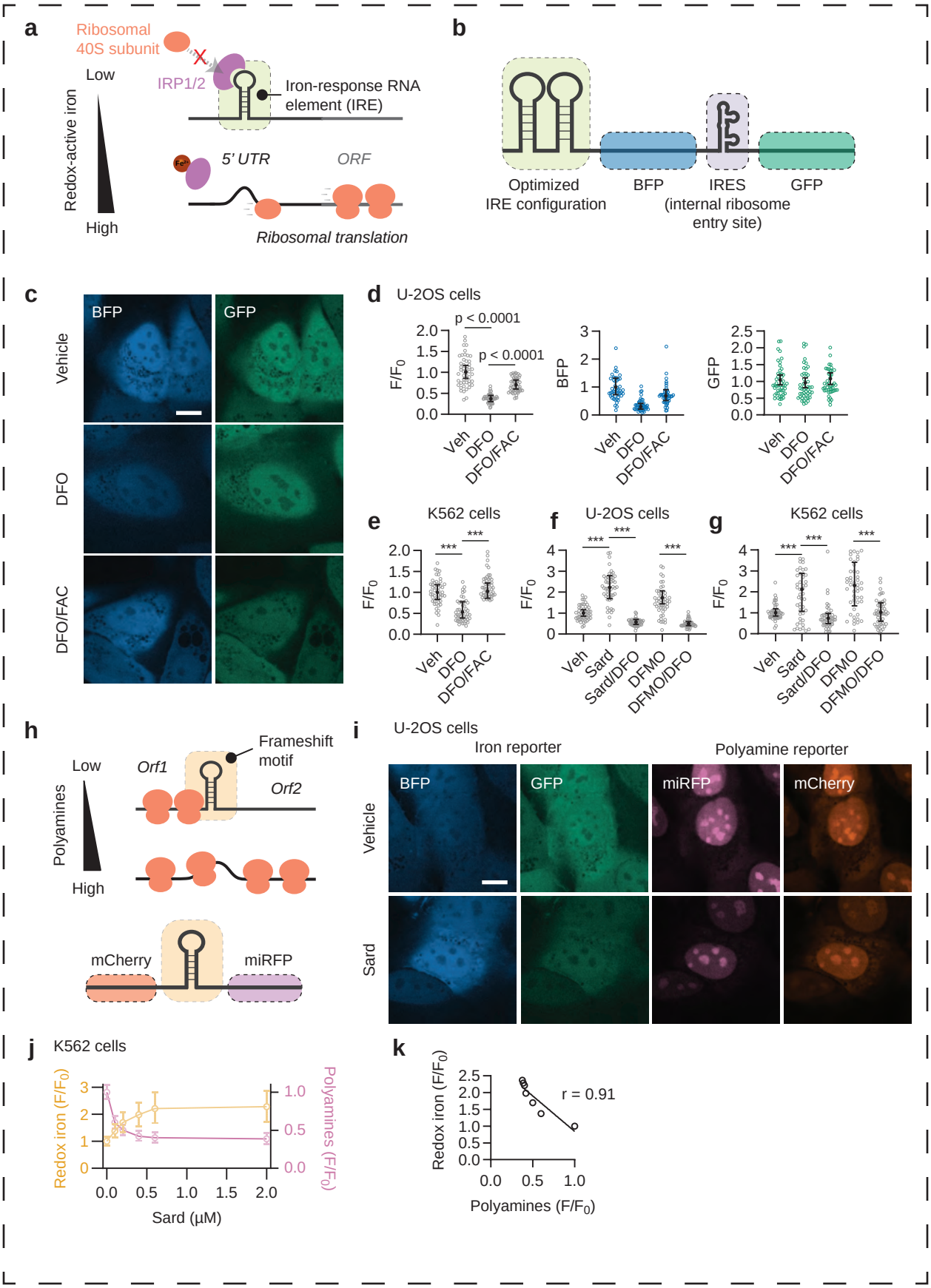

# Figure 6: Polyamines can chelate metal ions

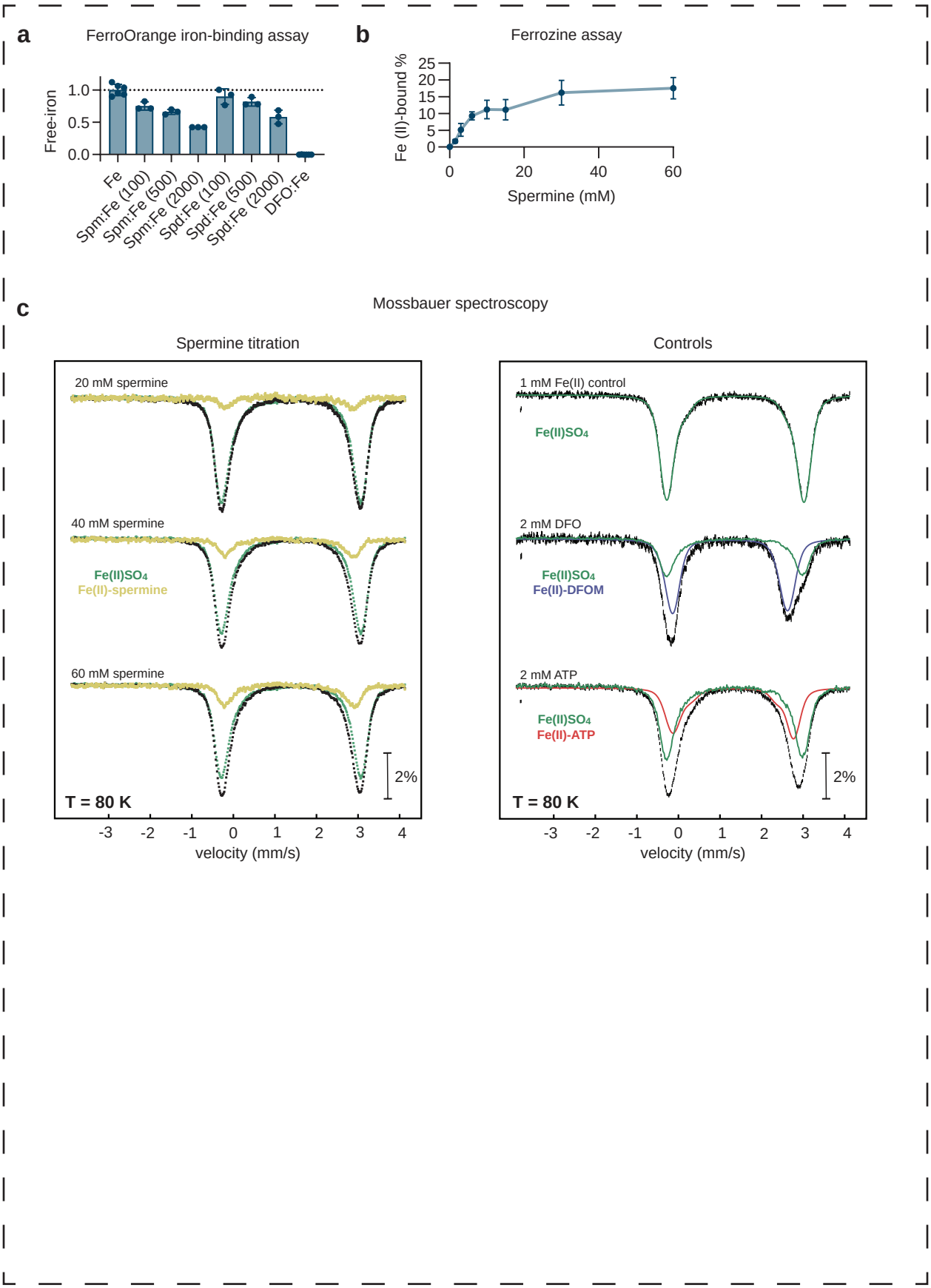
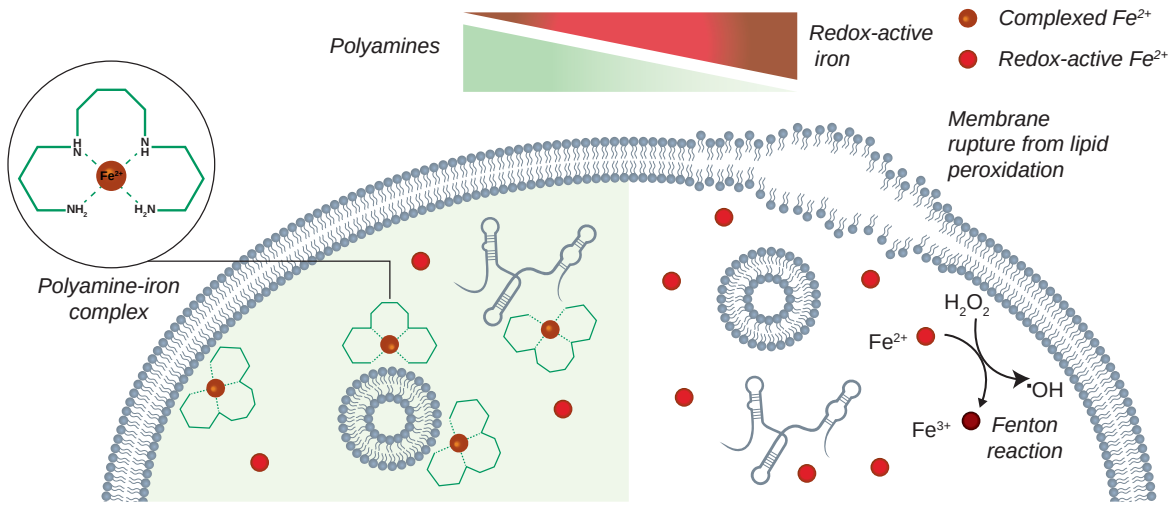
Figure 7: Polyamine depletion promotes ferroptosis